FEDERAL UNIVERSITY OF SANTA CATARINA

GRADUATE PROGRAM IN CHEMICAL ENGINEERING

Guilherme Patussi Goldschmidt

Silica-Based Glass Materials Manufactured by Colloidal Processing and 3D-Printing of Nano/Microsilica Powders

Florianópolis, 2020

Guilherme Patussi Goldschmidt

Silica-Based Glass Materials Manufactured by Colloidal Processing and 3D-Printing of Nano/Microsilica Powders

Master thesis for the degree of Master's in Chemical Engineering presented to the Graduate Program in Chemical Engineering at the Federal University of Santa Catarina.

Supervisor: Prof. Dr. Dachamir Hotza

Co-supervisors: Prof. Dr. Antonio Pedro Novaes de Oliveira and Dra. Elisângela Guzi de Moraes

Florianópolis

2020

Ficha de identificação da obra elaborada pelo autor

através do Programa de Geração Automática da Biblioteca Universitária da UFSC.

Patussi Goldschmidt, Guilherme
Silica-Based Glass Materials Manufactured by Colloidal Processing and 3D-Printing of Nano/Microsilica Powders / Guilherme Patussi Goldschmidt ; orientador, Dachamir Hotza, coorientadora, Elisângela Guzi de Moraes, coorientador, Antônio Pedro Novaes de Oliveira, 2020.
85 p.

Dissertação (mestrado) - Universidade Federal de Santa Catarina, Centro Tecnológico, Programa de Pós-Graduação em Engenharia Química, Florianópolis, 2020.

Inclui referências.

1. Engenharia Química. 2. Técnicas de Manufatura Usual e Manufatura Aditiva de Sílica. 3. Impressão 3D. I. Hotza, Dachamir. II. Guzi de Moraes, Elisângela. III. Novaes de Oliveira, Antônio Pedro IV. Universidade Federal de Santa Catarina. Programa de Pós-Graduação em Engenharia Química. V. Título.

Guilherme Patussi Goldschmidt

SILICA-BASED GLASS MATERIALS MANUFACTURED BY COLLOIDAL PROCESSING AND 3D-PRINTING OF NANO/MICROSILICA POWDERS

O presente trabalho em nível de mestrado foi avaliado e aprovado por banca examinadora composta pelos seguintes membros:

Prof. Dachamir Hotza, Dr.
Presidente da banca/Orientador

Prof. Antônio Pedro Novaes de Oliveira, Dr.
Coorientador - UFSC

Elisângela Guzi de Moraes, Dr.ª
Coorientadora - UFSC

Prof. João Batista Rodrigues Neto, Dr.
UFSC

Prof.ª Sabrina Arcaro, Dr.ª
UNESC

Certificamos que esta é a **versão original** e **final** do trabalho de conclusão que foi julgado adequado para obtenção do título de Mestre em Engenharia Química.

Documento assinado digitalmente
Debora de Oliveira
Data: 18/10/2020 18:09:19-0300
CPF: 728.453.929-15

Prof.ª Débora de Oliveira, Drª
Coordenadora do Programa de Pós-Graduação em Engenharia Química

Documento assinado digitalmente
Dachamir Hotza
Data: 18/10/2020 11:13:50-0300
CPF: 495.235.039-87

Prof. Dachamir Hotza, Dr.
Orientador

Florianópolis, 15 de Outubro de 2020.

ACKNOWLEDGEMENTS

A special “thank you’ for my advisor Prof. Dachamir Hotza for providing me with opportunities and knowledge throughout the whole MSc period. A great recognition for Prof. Jens Günster for having me in the Federal Institute of Materials Research and Testing in Berlin and Prof. Antonio Pedro Novaes de Oliveira for providing me with the tools to continue my research in Brazil.

The most grateful acknowledgement to Raphael de Melo Bernardino for helping me during my period in Germany and Dr. Elisângela Guzi de Moraes for all the support and experience for the research in Brazil.

Thanks to my family for the support as well as housing during my MSc period and the most special thank you to my girlfriend for her patience, support and companionship, both vital for the success of my research.

This study was financed in part by the Coordenação de Aperfeiçoamento de Pessoal de Nível Superior – Brasil (CAPES) – Project Nº CAPES-PRINT/88881.310728/2018-01.

RESUMO

O vidro, tal como o conhecemos hoje em dia, apresenta propriedades atrativas tais como dureza relativamente elevada, alta transparência, resistência térmica e química elevadas. Devido às suas características variáveis, existe uma grande atratividade para o desenvolvimento de materiais novos e avançados, através de técnicas de fabricação consolidadas e inovadoras. No presente trabalho a produção de vidro à base de dióxido de silício foi escolhido, dada a grande abundância na crosta terrestre e a sua multiplicidade de aplicações. Os objetivos deste trabalho consistiram em obter produtos à base de sílica a partir de dois métodos de produção: *slip casting* para vidro transparente e impressão em 3D para *scaffolds* com estruturas avançadas. As matérias-primas consistiram basicamente em nano (NS) e micro (MS) sílica amorfa e aditivos. Para *slip casting*, a suspensão foi preparada primeiro pela adição da NS em água, seguida por uma agitação mecânica por 4h a 1500 rpm. Em seguida, foi utilizada a técnica de sonicação por 30 minutos para evitar aglomeração e então a MS foi adicionada, com uma agitação por 3h a 1500 rpm. A suspensão foi vertida em moldes de gesso para o procedimento de *slip casting,* seguido de secagem, tratamento térmico, e depois polimento para obter o vidro transparente. Para a técnica de impressão 3D, foi produzido um novo pó com as matérias-primas (NMS). Foram preparadas duas suspensões: alginato de sódio e PVA, ambos com NMS. O processo consistiu na impressão das estruturas, seguida de secagem (temperatura ambiente e liofilização) e tratamento térmico. Os pós foram caracterizados: tamanho, com D50 de 227,8 nm para NS, 9,85 µm para MS e 7,47 µm para NMS, microestruturas (TEM/FESEM), e estabilidade térmica (DSC). As suspensões de *slip casting* e de *robocasting* foram estudadas quanto estabilidade através da reologia, com a observação de comportamento de *shear-thinning* para a suspensão de *slip casting*, bem como para as suspensões para impressão 3D. Os potenciais Zeta mostraram os valores de -30mV para NS, -50mV para MS e -35mV nos correspondentes pHs de trabalho. O material produzido por slip *casting* foi caracterizado quanto densidade com um valor resultante de 2,21 g/cm³ e propriedades ópticas, utilizando o índice de translucidez (TP) com um valor médio de ~38 % e de Opacidade de ~22 %, visualizando as possíveis aplicações ópticas relacionadas. Foram investigados os filamentos impressos quanto ao comportamento térmico utilizando dilatometria, mostrando que a suspensão de alginato de sódio encolheu cerca de 2% e o PVA cerca de 4%. A microestrutura das amostras impressas (disposição dos poros) foi avaliada com SEM, apontando a formação de porosidade unidirecional para estruturas de PVA. A densidade picnométrica foi de 2,41 g/cm³ para amostras de alginato de sódio com ~69% de porosidade e 2,41 g/cm³ com ~75% de porosidade para amostras de PVA. Os resultados foram exaustivamente discutidos, e foi fornecida uma ideia geral da taxa de sucesso. Para concluir, este trabalho dá uma visão geral da aplicabilidade da sílica como material de base para vidro transparente e *scaffolds* visando bioaplicações e abre possibilidades de maiores pesquisas nesses tópicos.

RESUMO EXPANDIDO

Introdução

A descoberta do vidro não apresenta dados precisos, mas aproxima-se, devido a descobertas de objetos vítreos nas necrópoles egípcias, que o material fora descoberto há pelo menos 5.000 anos e de forma casual. A produção de vidro como conhecemos hoje em dia teve início com o *boom* da revolução industrial e desenvolvimento de maquinário e os processos tradicionais praticamente mantêm-se os mesmos. O material como conhecemos hoje apresenta diversas propriedades atrativas, como dureza, transparência, resistência térmica e química. Devido à sua grande gama de propriedades, existe um grande atrativo na utilização e desenvolvimento de novos materiais, através de técnicas já consolidadas de manufatura e outras ainda em desenvolvimento. No presente trabalho optou-se por estudar a produção de corpos cerâmicos à base de dióxido de silício, devido à sua grande abundância na crosta terrestre e suas características compatíveis com diversos segmentos. Utilizaram-se matérias primas com dimensão micro e nanométrica e as técnicas de *slip casting* para a produção de corpos densos transparentes e de impressão 3D para obtenção de corpos biocompatíveis. Materiais transparentes a base de sílica são amplamente utilizados em muitas aplicações devido às suas características eletrônicas únicas, tais como baixa constante dielétrica, baixa perda dielétrica, alto ponto de fusão, alta resistência ao choque térmico e alta transparência para uma ampla gama de espectro de luz. Já os corpos 3D podem ser aplicados na área médica, como aparelhos de reparo ósseo ou sistemas de entrega de medicamentos como *scaffolds*.

Objetivos

Os objetivos gerais deste trabalho apresentam o foco de avaliar a obtenção de corpos densos transparentes por meio da técnica de *slip casting* bem como a impressão 3D de corpos cerâmicos com propriedades compatíveis com aplicações biomédicas. Como objetivos específicos: investigar a viabilidade da utilização de manufatura usual para a produção de vidro transparente, com o foco em aplicações em fibra ótica e vidro resistente ao choque, e avaliar a aplicação de manufatura aditiva visando a produção de *scaffolds*.

Metodologia

Para a elaboração da pesquisa foi realizada uma breve referência sobre as matérias primas, aplicações e utilizadas de materiais vítreos bem como das técnicas de manufatura e as caracterizações realizadas. O trabalho foi dividido conforme a metodologia de produção. Para a obtenção de discos transparentes foi preparada uma pasta com a nanossílica (NS) e a microssílica (MS) com água, a uma proporção de 70 % sólidos (9,2% NS e 60,8% MS) para 30% de água em massa. A suspensão foi despejada em moldes de gesso, secas por um período de 24 h seguido pelo processo de sinterização em etapas, até 1500 °C em um forno a vácuo.

Posterior a isso, os discos foram polidos com pastas e discos diamantados para remoção da rugosidade e formação de cristalinidade superficial proveniente da transformação de sílica amorfa em cristalina. Já para a impressão 3D, utilizou-se uma mistura inicial da NS com a MS em modelo de conformação (NMS) do tipo amora, com a incorporação de partículas menores (nano) na superfície das maiores (micro), para aumentar a estabilidade dos pós. Posteriormente, a suspensão foi preparada com utilização de dispersante e espessante para otimizar a reologia para o processo de impressão. A mistura sólido/líquido foi realizada com o pó NMS e uma solução viscosa de alginato de sódio e outro a base de PVA. O primeiro utilizou-se a proporção (em massa) 55:45 e o segundo de 65:35. As peças impressas foram secas a temperatura ambiente por 24 h bem como passaram pelo processo de liofilização pelo mesmo período, para evitar formação de trincas. Por fim, as peças foram sinterizadas em etapas, até a temperatura de 1200 °C.

Resultados e Discussão

Os pós foram caracterizados por: distribuição de tamanho de partículas por DLS e SLS, com um D50 de 227,8 nm para NS, 9,85 µm para MS e 7,47 µm para NMS, microestruturas usando TEM e FESEM, e estabilidade térmica através de dados DSC, a fim de verificar a possibilidade de alcançar os resultados esperados. A suspensão para *slip casting*, bem como para a impressão 3D foram estudadas quanto sua estabilidade através da reologia, avaliando viscosidade e tensão de cisalhamento, variando a taxa de cisalhamento. Análises de potencial Zeta mostraram valores de -30mV para NS, -50mV para o MS e -35mV para NMS, em seus correspondentes pHs de trabalho. Os produtos de *slip* casting foram caracterizados quanto sua densidade, com um valor resultante de 2,21 g/cm³ e propriedades ópticas, usando índice de translucidez (TP) com um valor médio de ~38 e de Opacidade de ~22 %, focando em possíveis aplicações relacionadas a propriedades óticas. Filamentos obtidos por impressão 3D foram investigados quanto seu comportamento térmico usando dilatometria, mostrando que a suspensão a base de alginato de sódio cerca de 2% e a base de PVA em torno de 4%. A microestrutura das amostras impressas (disposição dos poros) foi avaliada com SEM apontando a formação de porosidade unidirecional para estruturas baseadas em PVA. A densidade picnométrica foi de 2,41 g/cm³ para amostras de alginato de sódio com ~69% de porosidade e 2,41 g/cm³ com ~75% de porosidade para amostras à base de PVA. Os resultados foram exaustivamente discutidos, e uma ideia geral da taxa de sucesso foi fornecida. Para concluir, este trabalho, propõe-se uma visão geral da aplicabilidade da sílica como material de base para vidro transparente e *scaffolds* visando aplicações biológicas, abrindo horizontes para mais pesquisas nessa área.

Conclusões

O objetivo geral de obtenção de produtos através de diferentes técnicas de manufatura de materiais cerâmicos foi alcançado, tanto para a metodologia tradicional quanto para a impressão 3D. Os objetivos específicos também foram satisfeitos, visto que a utilização de *slip casting* para produção de discos transparentes apresentou boa reprodutibilidade com elevada transparência. Já para a manufatura aditiva, após a produção do pó NMS e testes com diferentes géis, foi possível a produção de uma tinta otimizada para o processo de impressão 3D. A utilização de diferentes processos de secagem permitiu a obtenção de produtos com características diferentes que podem ser exploradas conforme a aplicabilidade.

Palavras-chave: Sílica. Vidro. Materiais. Impressão 3D. *Slip casting*.

ABSTRACT

Glass as we know today presents appealing properties such as relatively high hardness, high transparency, thermal and very high chemical durability. Due to its varying features, there is a great attractiveness for the development of new and advanced materials, through consolidated and novel manufacturing techniques. In the present work silicon dioxide-based glass was chosen given the great abundance in Earth's crust and its multiapplication. The objectives of this work consisted of achieving silica-based products from two production methods: slip casting for transparent glass and 3D printing towards advanced structures/scaffolds. The raw materials consisted basically of nano (NS) and micro (MS) scaled amorphous silica and additives. For slip casting, the suspension was prepared firstly by the addition of the NS into water, followed by a 4h stirring at 1500 rpm. Next, a 30 min sonication was used to prevent aggregation and the MS added, with a 3h stirring and 1500 rpm. The suspension was poured into gypsum molds for the slip casting procedure, followed by drying, firing, and then polishing to achieve the transparent glass. For the 3D printing technique, a new powder was produced with an occlusion organization with the nano and micro silicas (NMS). Two suspensions were prepared: sodium alginate with NMS and PVA gel with NMS. The process consisted of printing the structures, followed by drying (room temperature and lyophilization) and firing. The powders were characterized for: their size, with a D50 of 227.8 nm for NS, 9.85 μm for MS and 7.47 μm for NMS, microstructures using TEM and FESEM, and thermal stability through DSC data, in order to ascertain the possibility of achieving the expected results. Slip casting suspension and robocasting suspension were studied for its stability through rheology with the observance of a shear-thinning behavior for the slip casting suspension, as well as for the suspensions. Zeta potential experiments showed the values of -30mV for the NS, -50mV for MS and -35mV at their corresponding working pHs. Slip cast glass was characterized for its density with a resulting value of 2.21 g/cm³ and optical properties, using translucency index (TP) with an average value of ~38 and % Opacity of ~22%, visualizing the optical related possible applications. 3D printed filaments were investigated for its thermal behavior using dilatometry, showing that sodium alginate suspension shrinked around 2% and PVA gel around 4%. The printed samples' microstructure (pores arrangement) were evaluated with SEM pointing the formation of unidirectional porosity for PVA based structures. Picnometric density was of 2.41 g/cm³ for sodium alginate samples with ~65% porosity and 2.41 g/cm³ with ~75% of porosity for PVA based. Results were thoroughly discussed, and a general idea of success rate provided. To conclude, this work gives an overview of the applicability of silica as the basis material for transparent glass and bio scaffolds and opens the possibility of further research.

Keywords: Silica glass, materials, 3D printing, Slip casting.

LIST OF FIGURES

INDEX OF TABLES

SUMMARY

1. INTRODUCTION AND OBJECTIVES

As the humankind developed, reports point out the usage of natural glass, especially Obsidian (volcanic glass), for the production of knifes, arrowheads and jewelry, before the production knowledge was developed. Historians suggest that Phoenicians were the first to produce in the region of Syria around 500 B.C. However, according to archeological evidence, the first man made glass occurred in Eastern Mesopotamia and Egypt at around 3500 B.C. The glass manufacturing as we know actually began at around 1890 with the boom of the industrial revolution and the development of machinery. [1]

Quartz glass is the purest form of silica (SiO_2) and therefore the most valuable and sophisticated variety. Optical fibers are used everywhere in the world and to be produced, extremely clear glass can be used, such as quartz glass, to transmit light across long distances. [2]

Glass presents many appealing properties, such as hardness, transparency, elevated thermal and chemical resistance. Because of them, it is an important material that can be used for the most different applications, such as chemical, biological, optical and photonics, as well as in microfluidic and biocompatible systems. Thus, there is a drive to achieve features in glass in nanoscale as well as in complex configurations that conventional glass processing techniques does not offer. [3]

Additive manufacturing (AM), commonly known as 3D printing, has been a novel technology in the most diverse fields, enabling the production of structures with unique properties, such as shape-morphing structures, soft robotics and biomaterial tissue constructs. The possibility to print glass can enable the production of functional glass materials combining attractive material properties with high and complex architectures. [3]

The idea of this research is to further study the possibility of diverse techniques and applications to use with silicon dioxide. For an overall idea, in the past 5 years, a few researches have approached this material differently. As an overview in the Additive Manufacturing segment, Zhu et al. (2019), have provided a review on multiple materials and techniques, with several mentions of silica as a partial or total raw material. Narrowing to the specific interest of silicon dioxide products, Peng et al. (2018), have worked towards an overlook regarding ceramic-based robocasting, with the mentioning of silica as one of the suggested materials for such technique. In an even further study, directing the focus for possible applications, Nguyen et al (2017), has performed 3D printing of transparent silica glass using tetraglyme and polydimethylsiloxane (PDMS) as additives. As regarding to medical applications, Lei et al. (2020) have provided a review in the same field of focus as the present dissertation. The paper further investigates biomedical applications of porous silica materials, giving emphasis to the fact that silica can be applied diversely in the medical segment, especially when porous. [3] [4] [5] [6]

The general objective of this work is to obtain silica-based glass materials from silica micro and nanopowder.

In this work, silica was used as a raw material to either traditional or advanced manufacturing techniques, in order to obtain different products.

In a more specific approach, the traditional slip casting technique was chosen to produce silicate transparent glass, which is widely used in many applications due to its unique electronic characteristics such as low dielectric constant, low dielectric loss, high melting point, high thermal shock resistance, and high transparency for wide range of light spectrum. [7]

As for an advanced processing technique, robocasting or 3D printing, was chosen. It allows for the product to be built without the assistance of a mold and to print advanced structures, which can then be used for medical applications, as bone-repairing devices or drug-delivery systems as scaffolds. [8]

2. LITERATURE REVIEW

2.1. Silicon Dioxide

Silicon dioxide (silica, SiO_2), usually found in nature as quartz, is one of the most abundant compounds on Earth, which corresponds to more than 10% of its crust. Silica is an inorganic material that occurs in nature in the form of rock and sand, varying its internal structure but always presenting the same chemical composition. The basic structure has a SiO_4 tetrahedron, which means that one silicon can bind four oxygen atoms and each oxygen two silicon atoms. As the chemical bonds between silicon and oxygen are covalent, crystalline silica has a high melting temperature (1713 ºC) and high chemical stability. [9] [10]

Structurally, silica can take two structural forms: crystalline and amorphous. The first one presents structures with repeating patterns of silicon and oxygen and is commonly found as quartz, which is the only polymorph structure stable on Earth’s surface. At higher temperatures, silicon dioxide also can occur at normal pressure in the tridymite and cristobalite forms, which are known to be found in volcanic rocks. As for the amorphous group, the internal structure is randomly linked. Figure 1 shows a silicon dioxide phase diagram of the most stable polymorphs at a given pressure, temperature and Earth`s depth. [9] [10]

Figure 1 - Silicon dioxide stable polymorphs phase diagram.

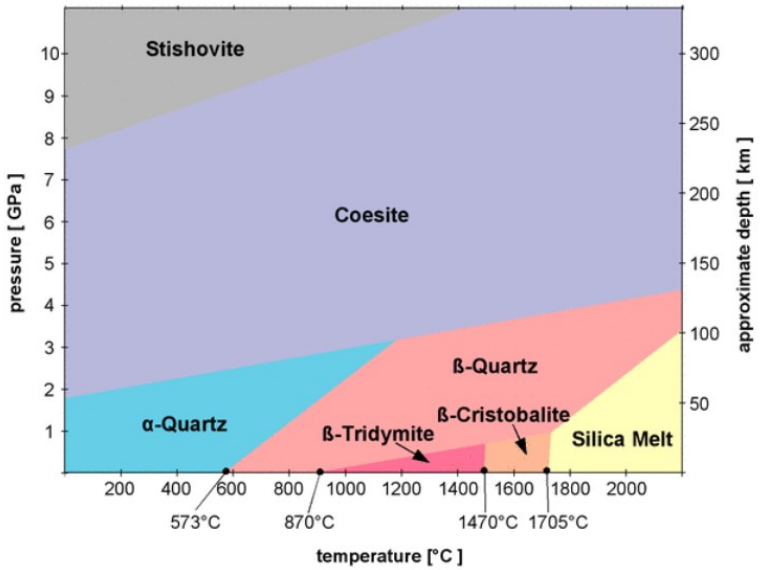

Source: http://www.quartzpage.de/gen_mod.html

Silicon dioxide can also be industrially produced and is referred to its amorphous form as “quartz glass”, “silica” or “fused silica”. It is generated by burning volatile silanes, such as silicon tetrachloride, in an oxygen-hydrogen flame, as it can be seen in Figure 2.

Figure 2 - Fumed silica production scheme.

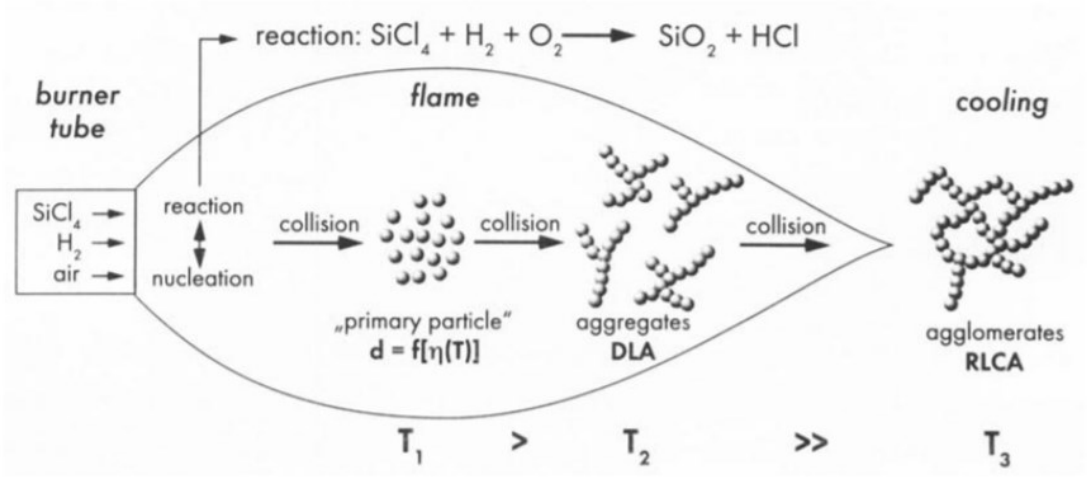

Source: [3]

An important aspect is that the final particle size is related to the flame temperature. At lower temperatures, collision and sticking particles results in partial fusion, which forms aggregates. They leave the flame and cool down, but still collide, resulting in the formation of agglomerates of aggregates, which are bond together by physical and chemical surface interactions. Thus, in order to obtain thinner silica particles, higher flame temperatures must be used, which result in higher costs of production and consequently more expensive products. [11]

This alternative route to obtain silica powder is due to the desired high purity (>99.5%), which is very rare in nature, especially when needed in higher volumes. Such grades of purity and homogeneity are particularly important in the production of transparent objects, to ensure good transmittance in ultraviolet, visible and infrared spectral range. It also presents great chemical resistance to most bases and acid, a high thermal resistance (>1000 ºC) and a high temperature shock resistance with a resulting low expansion coefficient. Such unique optical, mechanical and thermal properties made silica to be an extremely important material in the fabrication of high-tech products, including glasses and optical fibers. [2]

Ceramics, glasses and the combination of both include a great number of possible inorganic and nonmetallic blends. There are a broad range of applications for such materials, for example in the medical industry, these compounds have been key diagnostic instruments, chemical ware, thermometers, tissue culture and fiber optics for endoscopy. A more specific class, insoluble porous glasses have also been applied as carriers for enzymes, antiparts and antigens, due to their advantages of microbial attack resistance, pH changes, solvent and temperature conditions. Insoluble glasses have also been used as microinjectable delivery systems for *in situ* tumor treatments. [12]

Glass-ceramics are also widely used in the dentistry field as dental restorations, such as inlays and onlays, crowns and multi-unit bridges. The aesthetic and functional dentistry are two of the rapidly growing fields of biomaterials. [12]

2.2. Colloidal Processing

2.2.1. Stability and Rheology of Colloidal Suspensions

Before defining the term stability, it is important to understand what a colloid is. The term is used to describe particles that present at least one dimension between 0.001 and 1 μm. A distinguishing feature of the colloidal systems is that the dispersing medium and the particle's contact area is large. Therefore, the interactions resulting from interparticle and surface forces are strong contributors to the suspension's behavior. The study of such particles has led to innumerous technical advances in the most diverse fields, including ceramic processing, coatings, suspensions, drug delivery, food processing, among others. [13]

A colloidal suspension can offer different potentialities and reliability to produce ceramic films and bulk forms, as long as there is a careful control of the suspension structure and during the process development. This approach is constructed according to five steps: (1) powder synthesis, (2) suspension preparation, (3) consolidation to the desired shape, (4) removal of solvent phase and (5) densification to obtain the microstructure for optimal performance. Unintentional defects can occur during any of the steps and persist or be more noticeable during densification. Consequently, there is a drive toward continuous development in understanding of colloidal

stability and steps of the production process to achieve the desired microstructure and form, combining optimal performance and architecture to the desired product. [13]

The suspension's stability depends on the interaction between the particles, which can be separated into attractive and repulsive forces. The first one is due to the Van der Waals forces, responsible for separating the particles from each other. As the repulsion component, when there is a presence of a polar liquid, there is the presence of the electrical double layer. The suspension stability is only obtained when the repulsive forces are dominant over the attractive. This constitutes the electrostatic stabilizing mechanism, which can be achieved through pH, presence of electrolytes and surfactants. [14]

The suspension stability can also be achieved using different mechanisms, such as steric. It is obtained with the use of long-chain polymers adsorbed onto the surface of the particles, preventing the contact among each other. It is recommended for suspension's with high solids contents in a non-aqueous media. [14] An alternative is the electrostatic mechanism in which the attraction Van der Waals forces are counterbalanced by the repulsive Coulomb forces acting between the negatively charged colloidal particles. Another possibility to stabilize the suspension is through electrosteric interactions, which is a combination of both steric and electrostatic mechanisms. [14]

One way to analyze suspension stability is the zeta potential. To first understand this measurement, it is important to understand the Derjaguin–Landau–Verwey–Overbeek (DLVO). It states the total interaction energy is the sum of repulsive electrostatic double layer forces and attractive Van der Waals forces (Figure 3). In water the particles can present either neutral, positive or negative surface charges due to the reaction of neutral -OH surface sites with either H+ or OH-. In the isoelectric point (IEP), the amount of positive and negatives charges equals one another and result in a neutral surface. Ions with opposite charges (counter ions) create clouds around each particle. As a result, when particles approach each other, their respective counter ions clouds overlap, increasing the repulsive force. The separation distance where particles repel strongly each other is directly influenced by the effective thickness of the opposite clouds, which is related to the Debye length. The Debye length is inversely proportional to the amount of electrolyte concentration (presence of salts). At low salt concentrations the Debye length is sufficiently high that the repulsion forces overcome the attractive, resulting in a dispersed suspension. When the pH of the suspension is adjusted to the IEP, the absence of repulsion results in a strong network of particles and causes the agglomeration of slurries. [15]

Figure 3 - Interaction energy versus particle distance between two hard spheres.

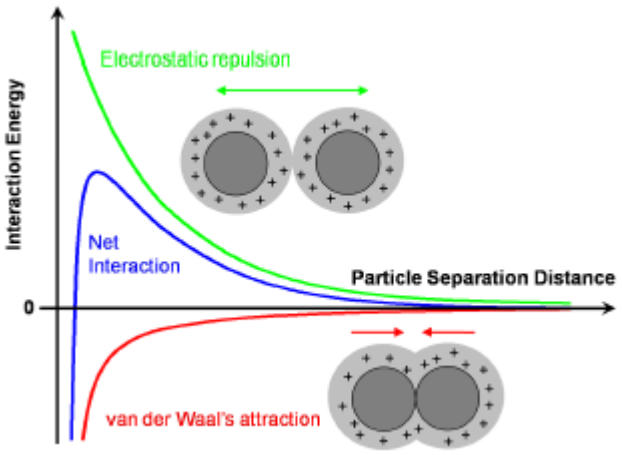

The electrostatic interactions can be indirectly determined by the surface charge of particles when suspended in a polar media, through zeta potential. This parameter cannot guarantee the stability of the suspension, but it can be used as a reliable tool to understand whether a suspension is stable or unstable, and its manipulation can be taken towards the desired direction. Zeta potential can be calculated according to Equation 1:

$$\mu_e = \frac{[2.\varepsilon.\zeta.f(k.a)]}{3.\eta} \qquad (1)$$

where:

ε = dielectric constant of the solution;

ζ = zeta potential;

η = viscosity of the suspension fluid phase;

f = Henry's function;

k = Debye length (1/k = electric double layer thickness);

a = particle equivalent spherical diameter;

μ_e = unitary electrophoretic mobility.

Following the DVLO theory, zeta potential can be understood as an indirect measure of the net charge, created from the particles in the polar suspension, either by the presence of ions or the dissociation of particles surface group. The larger the absolute value of a zeta potential is, the more stable the suspension's behavior. Through adjustment of the parameter it is possible to control the colloidal stability of ceramic suspensions. Values higher than +30 and lower than – 30 mV are understood as sufficiently high to promote stable water suspensions. This occurs because

particles of the same charge (negative-negative or positive-positive) repel each other and the resultant force is stronger than the tendency of aggregation promoted by the Van der Waals forces. [16]

Another important feature that must be taken into account when working with slurries is the rheology, which can be defined as the science of deformation and flow. It is a branch of physics responsible for revealing information regarding flow behavior of liquids and deformation behavior of solids, which consequently affects the properties of the green part. All forms of shear nature, which can be described rheologically, can be in either in between two extremes: flow of ideal viscous liquids on one hand and the deformation of ideal elastic solids on the other. The behavior of real materials is based on a combination of both extremes, in different proportions and thus, called viscoelastic. [17]

For ceramic suspension's processing it is essential to gather knowledge regarding the rheological properties, mainly because it allows predicting the after-processing properties. For the suspension characterization it is necessary to know the information about the viscosity, which is a measurement of the internal friction of liquid molecules that are subject to the flow of liquid counteracts. If a linear correlation between shear rate and shear stress exists, the suspension can be defined as Newtonian. If the correlation is nonlinear it can't be defined as Newtonian and can be further divided into time-dependent or time-independent flow. [18]

The time-independent flow is further differentiated into pseudoplastic (shear thinning) and dilatant (shear thickening). The first one can be observed as the red curves in Figure 4 and it is noticeable that the shear rate's slope, as shear stress increases, decreases, and the viscosity decreases. It is also possible to observe that it may need an initial shear stress to force the fluid to begin to flow. As for the shear thickening behavior (blue curve in Figure 4), the tendency is the opposite: as the shear stress increases, the shear rate's slope increases and so does the viscosity.

For some suspensions with particle interactions, they firstly need to be destroyed before the flow process begins. This happens when a certain stress, or the so-called yield point is reached. This can be seen in Figure 4 as the green curve, with a displacement in the shear stress axis. Such behavior is known as Bingham fluid. [19] Shear thickening behavior is not favorable for practical applications. Therefore, a lot of work has been conducted to erase or circumvent these unfavorable effects and one typical example is the mixing with smaller particles. In general, polydispersity reduces the shear viscosity at a given particle volume fraction. [20]

Figure 4 – Typical rheological behaviors: shear stress vs. shear rate (left); apparent viscosity vs. shear rate (right).

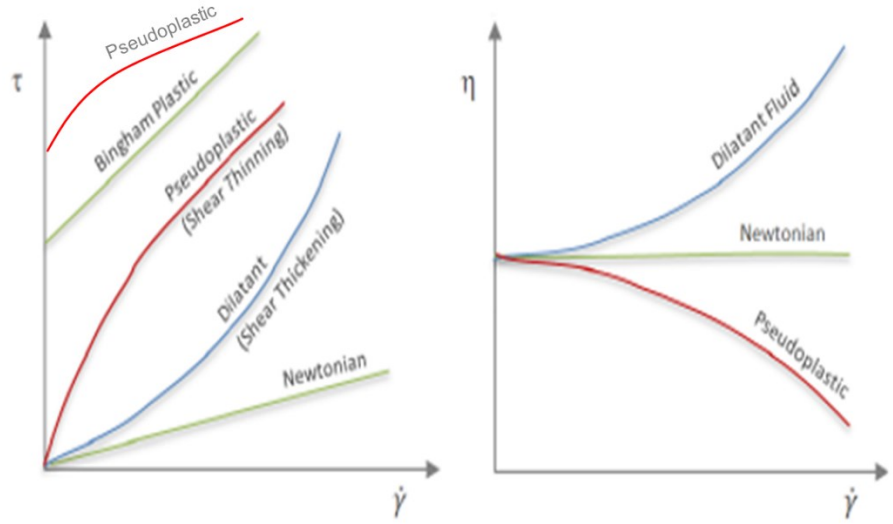

Source: [19]

A time-dependent flow is characterized by the fact that the viscosity changes during the shear stress. It can be divided into thixotropic and non-thixotropic (or anti-thixotropic) behaviors, which can be seen in Figure 5.

In thixotropic materials, the material structural strength decreases while shearing and can recover after a period of resting. As it can be seen in the graphic to the left of Figure 5, the stress is applied until a certain point, which causes the viscosity to decrease over time at a constant shear rate, turning the suspension thinner. This property is significant to products such as coatings and paints. [21]

In comparison, the non-thixotropic behavior can be observed in the Figure 5 on the right, in which the shear stress increases over time at a constant shear rate and the sample becomes more viscous. This occurs due to the additional connections between particles. This phenomenon is always observed simultaneously with the dilatant behavior and is caused due to the change of inner structure during the stress. It is considered reversible as soon as the applied outside force is removed. It can be observed in suspensions such as gypsum and water. [21]

Figure 5 - Time-dependent rheological behaviors: thixotropic (left) and anti-thixotropic (right).

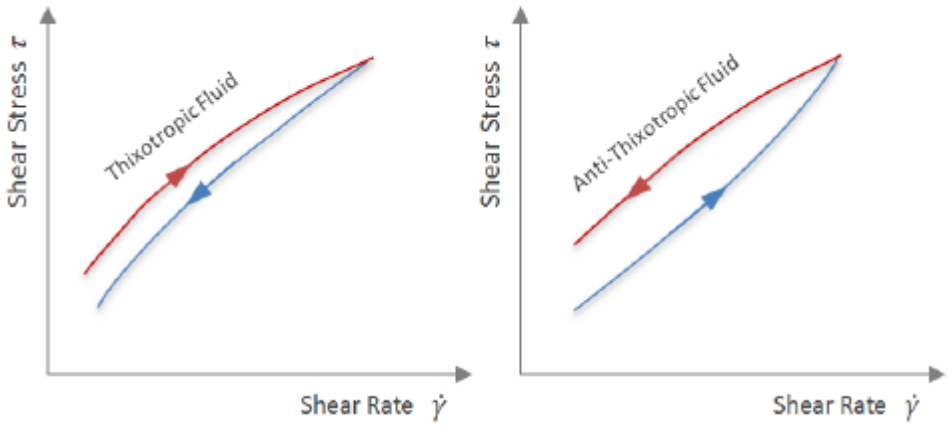

Source: [19]

Physical particle interactions and the operating shear rate ranges are the two main factors that affect the solids concentration when one determines suspension viscosities. As the suspension solids loading are increased, so is the viscosity. This phenomenon carries the relation to the physical particle interactions that occur when a solid is dispersed in a liquid and there are three main categories: interparticle attraction, hydrodynamic interactions and particle-particle contact. The first one promotes the formation of flocs and aggregates as is mostly common in fine particle suspensions. The second one is related to viscous dissipation in fine particle suspensions and the third carries information regarding frictional interactions. The effects intensities vary according to the suspension's concentration: at low solids concentration viscosity appears to increase linearly with the addition of solids until a threshold, in which the viscosity of the suspension increases significantly with small increments of concentration. Working on low-medium concentrations, the hydrodynamic interactions are dominant. For suspensions of medium-high solids loading, particle frictional contact is dominant, thus, the increase in viscosity. [22]

Another important point is that at a constant solids concentration, a reduction in the particle size will result in an increment in the suspension viscosity. This property is attributed to the increased surface area, which binds the solid-water molecules and consequently raises the viscosity. [22]

2.2.2. Slip, Pressure and Centrifugal Casting

Before introducing novel processing technologies, an overview of usual and consolidated colloidal processing techniques for the production of ceramics is important. They are used to produce complex ceramic shapes from a variety of raw materials, such as silicon carbide, silicon dioxide, clay and alumina. Conventional colloidal processing techniques are also known as casting, such as slip, pressure and centrifugal casting. All methods are based on the formation of a green part by a solid-liquid separation of a slip, which is a fluid suspension of colloidal ceramic particles (suspension). [23]

Slip casting, as shown in Figure 6, was the chosen forming technique to be used in this research work, due to its reliability, simplicity and low-cost

Figure 6 - Slip Casting technique.

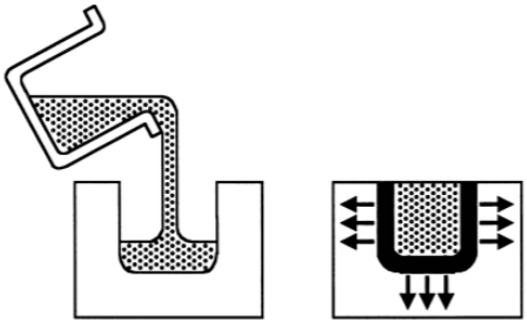

Source: [23]

The process starts by pouring a slip, usually aqueous, into a permeable mold, most often gypsum. The gypsum pores are much smaller than the particles in the slip and they work through capillary suction, removing the interparticle liquid from the slip. Consequently, a densely packed specimen is formed. The parts are separated from the gypsum mold and are often polished to remove any possible contaminations from the mold. This method is the most common industrial way of processing colloidal materials (in particular those parts with very complex shapes) and is has been used as a base technique to produce tableware, structural tubing, automotive and biomedical components, artware, and so on. [23] Further description is given in the following topics.

Complementary to the slip casting processing, the pressure casting resembles the first. It is an automated production operation, which diverges on the fact that the slip is pressurized to increase the filtration rate. The working principle is the same as slip casting. In this case, the suspension is filled into the containment, followed by the pressurizing gases and the moving plate drops, in order to produce the pressure. There are usually two main types of pressure-casting equipment: medium pressure (0.3 – 0.4 MPa) and high pressure (up to 4 MPa). As it is to expect, the higher the pressure, the higher production cost and consequently the more expensive the products. Medium pressure is used on large production of articles like sanitaryware and consists of assembling a series of stacked molds (gypsum or plastic) that are simultaneously pumped in with the slip. On the other hand, high pressure is more advantageous for lower production volume and smaller shapes, due to the fact that it works often one mold at time. Another peculiarity is that gypsum molds can’t be used, as they tend to fracture, being substituted by high-strength plastic. [23]

An alternate colloidal processing technique is centrifugal casting. It is the least common industrial method, because it requires a solid-liquid separation by applying centrifugal forces into the cast mold in a centrifuge. The slip is filled into the mold that is then rotated by the use of a motor and

auxiliary rollers on the top and the bottom. The molds, unlike the other two techniques, are not necessarily porous, being able to be made of various metals and plastics. The interparticle liquid in centrifugal casting is removed through the top of a cake, presenting lower packing density, compaction stress and thus higher in permeability than regions of a cake that are more distant from the center of rotation. Through centrifugal casting is possible to achieve significantly thicker shapes more rapidly than the other two techniques. It is important to notice that differential sedimentation velocities must be applied to avoid segregated microstructures that are prone to cracking during post processes, such as drying, debinding and sintering. [23]

2.3. Additive Manufacturing

Additive manufacturing (AM) is a method of producing objects from a digital model by depositing the constituent materials in a layer-by-layer manner using digitally controlled and operated devices and machinery. [24] AM technologies have reached an advanced level of maturity for several metallic and polymeric materials, while the ceramic field is still in development. [25]

A broad range of AM production methods have been applied to ceramics, each of them presenting specific advantages and limitations. Currently working technologies already provided means to produce relatively small and precise parts with a dense microstructure (especially through Stereolithography), scaffolds and log-pile structures with a designed porosity (using robocasting). However, for ceramic materials there is no well-established AM method capable to produce medium and large monolithic parts (can be understood of wall thickness being superior to 10–20 mm), with high density and properties comparable to standard processing technologies. For polymeric and metallic materials, powder bed-based AM is being used to provide the results. [25]

Among the many possible AM techniques, some of those are presented in Table 1 and are further described. Three different types of raw materials can be used: liquid, filament/suspension, or powder, each one more suitable to the respective printing technique. [26]

Table 1 - Additive manufacturing techniques.

Raw Material	Process	Material
Liquid	Stereolithography (SLA)	Photosensitive polymers
	Multi-jet Modeling (MJM)	Photosensitive acrylic, plastics and waxes
Filament/Suspension	Fused Deposition Modeling (FDM)	Thermoplastics
	Robocasting (RC) or Direct Inkjet Writing (DIW)	Ceramic suspension
Powder	Selective Laser Sintering (SLS)	Carbon Fiber, Aluminum, Polystyrene
	Selective Laser Melting (SLM)	Metals

Source: [26]

2.3.1. Stereolithography

Stereolithography (SLA) is considered to be the technology that started the revolution of rapid prototyping. It is the production of a three-dimensional object by photopolymerization of a liquid resin on a platform, as sketched in Figure 7.

Figure 7 - Stereolithography scheme.

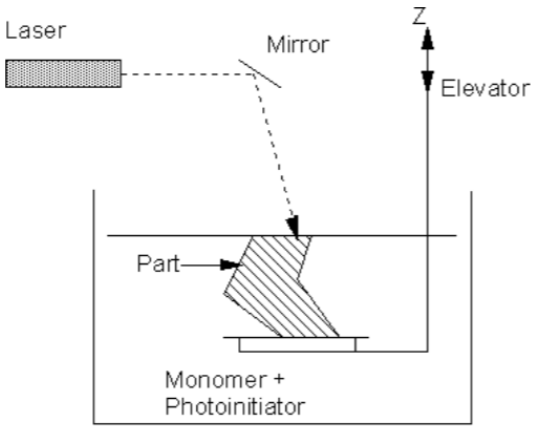

Source: [27]

A He-Cd or Argon-ion laser hits a mirror that is directed towards the support, where it traces a shape at the surface of a bath of photopolymerizable monomers. As the layer is completed, the elevator drops the support platform by one-layer thickness, another quantity of monomer is swept across the new solid surface and the process repeated. The parts are completed when the complete part is drawn and dried. The platform is raised, and the completed printed part removed. [27] This technique has been applied to a great range of products for prototyping, rapid tooling, design, scale, and exhibition models, optics and transparent covers. [28]

2.3.2. Multi-Jet Modeling

Multi-Jet Modeling (MJM), an alternative AM technique, is described in Figure 8. It works using a print head that selectively deposits materials on a platform. The droplets are usually a mixture of photopolymers and a second support material, such as waxes. After the deposition, an ultraviolet light solidifies the material to shape the cured parts. At the end, the leveler goes through the surface to levels the material and ensure a flat surface is formed. For this technique, after the parts are printed, an extra process is needed to remove the supporting material. When comparing to other techniques, MJM presents a high accuracy and surface finish and the possibility to use multiple materials and colors on the same part. The disadvantages consist of the limited range of usable materials and the relatively slow building process. [29]

Figure 8 - Multi-jet Modeling scheme.

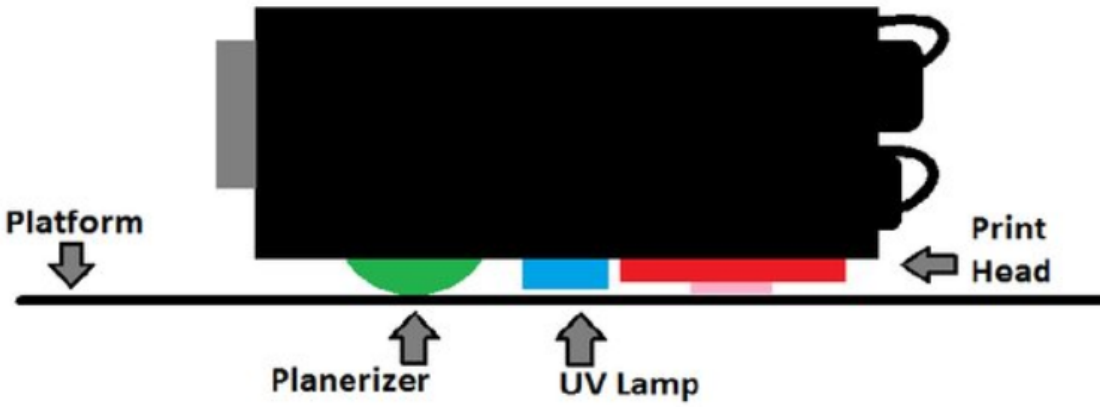

Source: Tolerance Analysis of 3D – MJM parts according to IT Grade

2.3.3. Fused Deposition Modeling

As for the filament/suspension techniques, the principle is the same, what diverges from one another is the kind of material used to print. The first one to be investigated is Fused Deposition Modeling (FDM), in which an object is created directly from a computer-aided design (CAD) model, using a feedstock to deposit layer-by-layer plastic filament material extruded through a nuzzle. It is one of the pioneers of AM processes. A schematic of the FDM fundamentals can be seen in Figure 9. [30]

Figure 9 - Fused Deposition Modeling scheme.

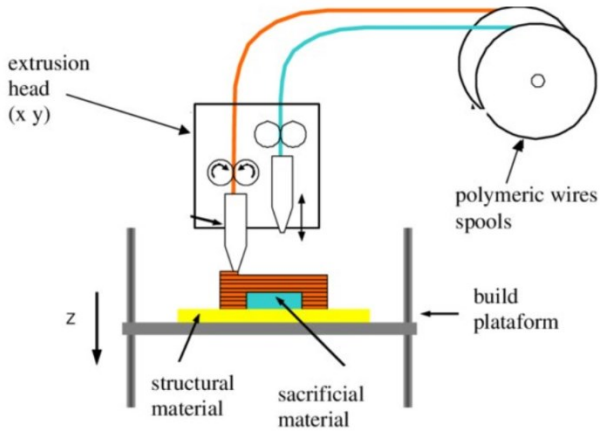

Source: https://www.researchgate.net/publication/269275574_EXPLORING_THE_CAPABILITIES_OF_THE_RAPID_PROTOTYPING_TECHNOLOGIES-SLS_AND_FDM

The principle of the FDM machine starts by the thermoplastic filament being drawn from the feedstock into the FDM liquefier, in which it is heated into a semi liquid state, to be extruded out through the orifice of a nozzle, fitted at the bottom of the head. A feedstock filament of support material is drawn from another deposit and through another nozzle tip if the design requires. The head works under the control of a computer and deposits the material in thin layers on the platform. The parts are created as the material solidifies almost immediately after being deposited by the nozzle and bonds to the previous layer. The parts can be removed after the deposition is done and the support material be removed mechanically or applying a solvent. The quality of the final parts is defined by the printing parameters and the printing capability of the FDM machine. [26] Due to safety, efficient operation, durability, low cost and its ability to process thermoplastics, it is one of the most widely used 3D printing techniques for functional prototypes. It is commonly used in quality and process improvement, new materials development, applications in biomedical and tissue engineering, as well as to produce the most variable tooling. [30]

2.3.4. Direct Suspension Jet Printing

Another suspension-based printing technique is Direct Suspension jet Printing (DIP), also known as Robocasting. DIP is an AM technology in which cross-sections of a three-dimensional model are deposited on top of each other on a substrate, in order to achieve the final object with a controllable geometry and composition. For this process, a ceramic colloidal suspension (suspension) is used, as shown in Figure 10.

Figure 10 - Direct Suspension jet Writing Scheme.

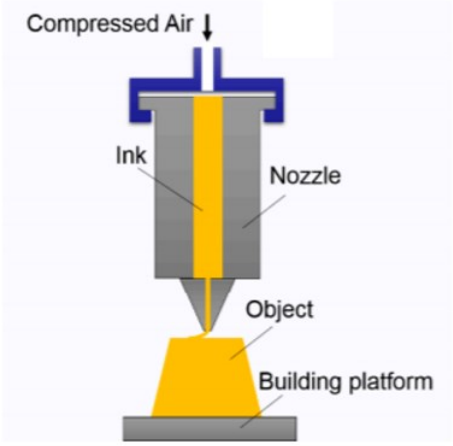

Source: 3D Printing Technologies for Flexible Tactile Sensors toward Wearable Electronics and Electronic Skin

The process methodology is based on subsequent depositions of single slices that are printed upon each other and are individually dried, followed by sintering of the complete part. Comparing DIP to other AM technologies, the materials produced by the first can be characterized by a low

thickness of the single layers and a high lateral resolution. Thus, components with high surface quality and outstanding shape accuracy can be reached through robocasting. [31] The robocasting technique was the chosen Additive Manufacturing to be further used in this research, as it is the most suitable for the used material, as well as the available technology to work with.

2.3.5. Selective Laser Sintering/Melting

Regarding powder-based printing techniques, two of them will be discussed. It is important to point out that the working principle of both Selective Laser Sintering and Melting are roughly the same but differ in a few technical details.

Selective laser Sintering, (SLS) uses a laser as the power source to sinter directly a powder, heating it just below the melting point. This occurs by pointing the beam towards the points in the space in a platform, defined by a preconstructed 3D model, binding the material together to create a solid layer. A model of SLS is shown in Figure 11. [32]

Figure 11 - Selective Laser Sintering Scheme

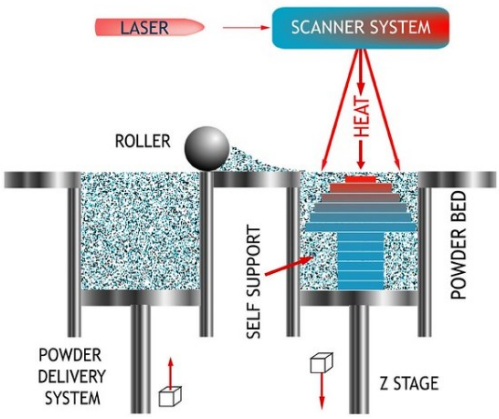

Source: https://www.flickr.com/photos/organ_printer/878476066

The principle is that the powder is taken from a reservoir and carried by the roller to the powder bed. The laser hits the scanner system that directs the heat towards the platform, heating and sintering the powder. This process occurs until all the 3D design is completed. [28] As it is common to the AM technologies, the platform is then lowered, and a new layer printed. The parts are then cooled down in the platform before being removed. A SLS characteristic is that it doesn't require the use of additional supports or support material. In its range of applications, it can be used to print a variety of objects, such as plastics, glass, ceramics and metals. It has proven to be a very helpful technique for industries that need only a small quantity of materials with high quality. For example, the aerospace industry is using this technique to build prototypes for airplane parts. [33]

Selective Laser Melting is very similar, being considered as a subcategory of SLS. Figure 12 shows how the printing technology works.

Figure 12 - Selective Laser Melting Scheme.

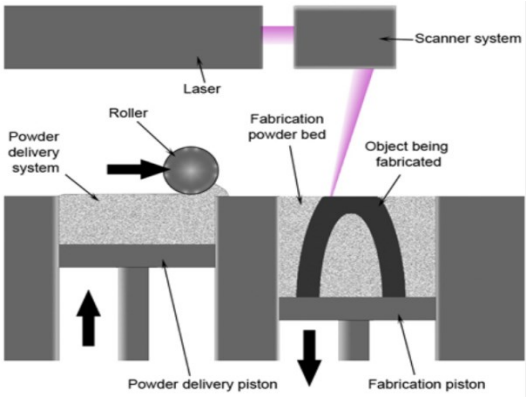

Source: https://commons.wikimedia.org/wiki/File:Selective_laser_melting_system_schematic.jpg

The printing process starts by the deposition of a thin layer of metal powder on a substrate plate in a building chamber. A high energy density laser is used to melt and fuse selected areas according to the previous 3D design CAD model. Once the layer is completely scanned by the laser, the platform is lower, a new layer of powder is loaded, and the process repeated. Processing parameters (laser power, scanning speed, layer thickness) are adjusted to ensure that a single melt vector can fuse completely with the nearby melt vectors and the preceding layer. After the scanning is completed, loose powders are removed from the chamber and the part can be removed from the platform. [34]

2.4. Optical Properties of Ceramics

Optical properties are important for transparent ceramics. It defines how a material interacts with the light and for this work should be approached. When the light falls on a surface, it interacts with the material. The type of interaction that occurs depends both on the wavelength of the light and the nature of the material and can take the form of reflection, transmittance or adsorption. For this work, transmission as an interaction is in the foreground, so this topic deals exclusively with transparency and translucency as properties. [35]

The physical property of transparency is that light passes through a material without scattering or adsorption. This property makes materials such as window glass or lenses appear clear and transparent to the eye. In contrast, in a translucent material, the photons of light are scattered internally or at the interface, resulting in a change in the refractive index. The object is only partially transparent. The refractive index can be used to define the strength and direction of light refraction at the transition from one medium to another. The smaller the refractive index, the lower the scattering of the material and the more translucent or transparent a material appears. [35]

In the production of transparent parts, porosity also plays an important role as an internal factor, since each individual pore represents an interface between two phases. At this interface there is a change in the refractive index and consequently reflection. This leads to a partial opacity or opaque object. A second phase can also lead to light scattering. For this reason, it is necessary to use high-purity raw materials, ensure a good material dispersion and to avoid possible impurities and large amounts of additives. Apart from the internal factors, external factors can also have an effect on transparency. The firing temperature is a key aspect, as normally transparent ceramics require a higher sintering temperature than ordinary ceramics, to remove porosity, As well as the temperature, the gas used during sintering affects directly in the aspect of the part. Using an inert gas medium or in air, because they might remain inside the pores of the part. To avoid such problem, hydrogen or vacuum atmospheres should be chosen. After all these requirements being fulfilled, there are still the final part structure. The transparency depends on the thickness and the surface condition of the sample at the same time. For example, light is reflected and diffused more strongly on a rough surface than on a smooth one. In general, the following relationship applies to the interactions between light and matter; transmission + absorption + reflection = 1. Absorption is not relevant in the context of this work, since high-purity material is used. [36]

3. MATERIALS AND METHODS

3.1. Materials

The materials used in this research work can be separated in three major categories: powders, additives and gels. The first refers to the solid's composition of the final parts and are responsible for the typical applications of the material developed. The second category is responsible for allowing or facilitating the production, changing rheological properties, increasing stability and so on. And the latter regards the liquid composition of the material.

3.1.1. Powders

Nanosilica (NS) powder (HDK S13, Wacker) was produced via flame hydrolysis. It is a loose bulky white powder, which presents chemical stability, heat and electric inertia and has no known health effects. It has a large specific surface area, resulting from the microscopic structure. [37] The data sheet of the material is available on the company's website and is displayed in Table 2:

Table 2 – Nanosilica (NS) technical data.

Feature	Value
SiO_2 content (based on the substance heated at 1000 °C/ 2 h)	>99.8%
Loss on Ignition at 1000 °C/2 h (based on the substance dried at 105 °C/2 h	<2%
Density at 20 °C	~ 2.2 g/cm³
Refraction Index at 20 °C	1.46
Silanol group density	2 SiOH/nm²
BET surface	110 – 140 m²/g
pH value (in 4% aqueous suspension)	3.8 – 4.5
Tapped density	~50 g/L
Loss on Drying (2 h at 105 °C)	<1.00%
Sieve residue (>40 µm)	<0.03%

Source: https://www.wacker.com/cms/en/products/product_groups/hdk.jsp

It is ideal for adjusting flow properties of liquids and giving powders optimum free flow. It is used in printing suspensions, paints, animal feeds, adhesives, natural and synthetic rubbers and many other applications. [37]

The microsilica (MS) powder (MKC, Mitsubishi Chemical) is an ultrapure synthetic silica derived from silicon alkoxide and ideal to be used as a raw material for quartz glass. It can be applied to optical fibers and parts of semiconductors. [38] The data sheet available on the company's website is displayed in Table 3.

Table 3 – Microsilica (MS) technical data.

Feature	Value
Visual Aspect	Off-white
Loss on Ignition	<10%
Molecular Formula	SiO_2
Average particle size (µm)	<45
Bulk density (g/cm³)	1.25
Purity (%)	99.5

Source:https://www.sigmaaldrich.com/Graphics/COfAInfo/SigmaSAPQM/COFA/34/342890/342890-BULK_____MKCG4754__.pdf

3.1.2. Additives

An ammonium salt of a polyelectrolyte (Duramax D-3005, Dow Chemical) was used as dispersant. It presents low molecular mass that allows it to be effective at low levels and also eliminates change of slip viscosity with time due to dispersant adsorption. It is supplied as a 35% wt suspension in water. [39] Respective technical data can be found in Table 4:

Table 4 – Dispersant (Duramax D-3005) technical data.

Feature	**Value**
Visual Aspect	Pale yellow liquid
Total Solids (%)	35
Molecular Mass (Da)	2400
Density (g/cm³)	1.16
Viscosity (Brookfield #1, 60 rpm) (mPa·s)	<100
pH	6.0-7.0
Residue After Firing (%)	2.7 (air)
Ionic Form	Ammonium salt

Source:https://nshosting.dow.com/doc-archive/business/pmat/duramax/duramax_d-3005/tds/duramax_d-3005.pdf

A water-soluble cellulose ether polymer based on non-ionic methylcellulose (Methocel A4M, Sigma Aldrich) was used as binder. [40] Some technical information of this additive can be found in Table 5:

Table 5 – Binder (Methocel A4M) technical data.

Feature	**Value**
Visual Aspect	White to off-white
Molecular Mass	88.000
Density (g/cm³)	0.7
Viscosity (2% aqueous at 20 ºC) (mPa·s)	3500 - 5600
Methoxyl (%)	27.5 – 31.5
Sodium Chloride (%)	<1.5

Source: https://www.chempoint.com/products/dupont/methocel-water-soluble-cellulose-ethers/methocel-water-soluble-cellulose-ethers/methocel-a4m

A more viscous suspension than water was necessary in order to prepare the suspension with adequate rheological characteristics for 3D printing. In this case, sodium alginate and PVA (polyvinyl alcohol) were used as raw materials for the liquid portion.

Sodium alginate (Sigma Aldrich) is an anionic copolymer manufactured from brown algae. The seaweed is extracted with a dilute alkaline solution, which causes the solubilization of the alginic acid present. [41] Some technical information of the material can be found in Table 6:

Table 6 – Viscous suspension precursor (sodium alginate) technical data.

Feature	**Value**
Visual aspect	White to beige and faint brown to light brown
Physical state	Solid
Loss on Drying (%)	<15.5
Viscosity (1% water) (mPa·s)	5.0–40.0
pH (1% water)	5–8

Source: https://www.sigmaaldrich.com/catalog/product/aldrich/w201502?lang=pt&region=BR

PVA (Sigma Aldrich), a synthetic water-soluble polymer is produced by dissolving Polyvinyl acetate (PVA) in alcohol (methanol, for example) and the addition of an alkaline catalyst (sodium hydroxide, for example). The hydrolysis removes the acetate groups from PVA molecules without damaging the long-chain structure. If the reaction is completed, the product is highly soluble in water and insoluble in practically all organic solvents. [42] Technical information can be found in Table 7:

Table 7 – Viscous suspension precursor (PVA) technical data.

Feature	**Value**
Visual aspect	Off-white
Hydrolysis (%)	85-89
Loss on Drying (%)	< 0.9
Viscosity (4% water) (mPa·s)	3.5-4.5
pH (4% water)	4.5-6.5

Source: https://www.sigmaaldrich.com/catalog/product/aldrich/363170?lang=pt&region=BR&gclid=CjwKCAiAnfjyBRBxEiwA-EECLCCAM9OxG_udpZZHUFBVwPa9mFzRijg3ooI0b9naS9rwBN_oPN-aohoCTQAQAvD_BwE

The preparation of the sodium alginate (6 wt.% concentrated) solution consists of mixing the gel-former with distilled water heated up to 60 ºC, in order to obtain a gel. The homogenization was performed in a magnetic mixer (Magnetic stirrer IKA, with an RCT Basic heating) at 350 rpm, until

the solids are completely dissolved. After cooling, the alginate gel was stored at lower temperatures to preserve the gel properties, as it is based on previous experience from the research group.

As for the PVA (20 wt.% concentrated) solution preparation, was carried out in a water bath at 90 ºC, followed by the addition of 2 mL of isopropyl alcohol, in order to avoid lumps formation. The viscous suspension, PVA, was then added at the liquid and stirred (Magnetic stirrer IKA, with a RCT Basic heating) at 350 rpm, until the gel is completely cooled down to room temperature (~25 ºC).

3.2. Methods

The procedures of this research can be separated into usual colloidal processing, through slip casting, and novel ceramic shaping, through robocasting. This was done due to the different applications designed for each process, in order to provide results in more than one field, showing the versatility of silicon dioxide compounds. Both techniques are further described with a more specific and tailored approach. Later, sintering procedure and characterization methods are also described in detail.

3.2.1. Shaping

3.2.1.1. Slip Casting

The slip casting procedure can be divided into three different parts, in order to fully understand the process: firstly, the mold should be built. Secondly, the suspension composition should be determined and prepared to then, lastly, proceed to the casting itself and the parts production.

Slip casting started by the preparation of the gypsum molds. [23] To do so, a solid: water volumetric ratio of 1.5:1 was chosen [43]. The mixture is poured into a suitable container with a diameter of 25 mm ± 0.3 mm and a height of 7 mm ± 0.05 mm. After the plaster has cured, it is carefully removed from the vessel and polished with sandpaper. It is then divided into two halves by an electric saw, so the green parts can be easily removed without any damage, as it can be seen in Figure 13. The final step is to dry the molds to ensure there is no residual water, and to do so, a muffle oven at 50 ºC was used for a period of 24 h.

Figure 13 – Photography showing the gypsum mold produced and used for slip casting.

The actual production of the desired product is conducted after the molds are ready. A simplified process diagram can be seen in Figure 14 and is further explained in the subsequent text.

Figure 14 - Slip casting simplified flowchart.

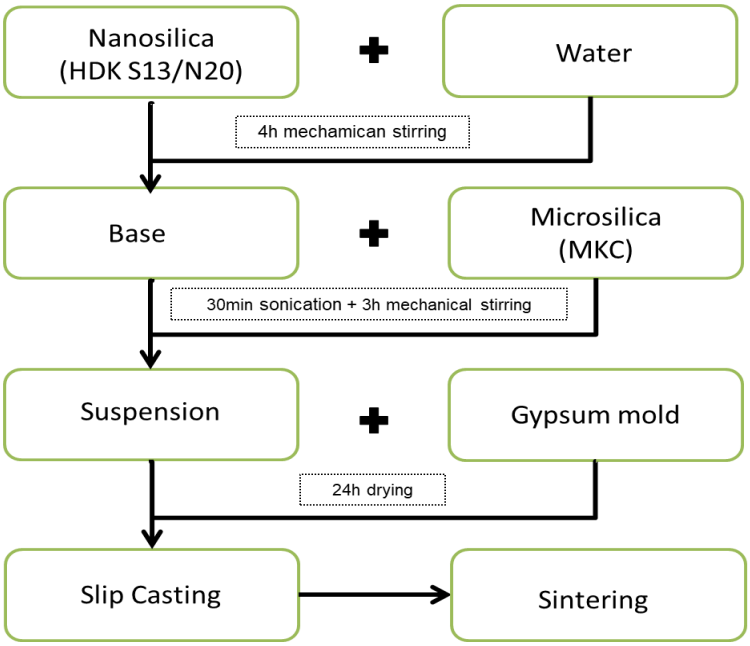

The suspension, or slip, was prepared and in order to do so, a series of research was performed to ensure a better understanding when developing the ideal solids concentration, as well as the production steps. It is desirable for robocasting slurries that have solids loading close to the dilatant transition, so that with minimal drying a printed layer becomes structurally consistent and can act as a foundation for the subsequent layer. [5]

The suspension was obtained through the mixture of silica powder of two different particle sizes (nano and microsilica) and deionized water. The used materials as well as the compositions were determined from previous experiments as well as based on the research proposed by [19]. The objective to use NS and MS powder is to obtain highly compacted suspension, in which the bigger pores are filled with smaller particles resulting in a less porous suspension and consequently a denser material.

The suspension preparation is performed in two main steps: firstly, mixing the water with NS (base) and followed by MS addition (final suspension). To prepare the base, the nanopowder is massed and the respective quantity of water is added in the Teflon recipient in which is mixed. In order to obtain a homogeneous suspension, the NS is added gradually to water, alternating with hand mixing and later using the mixer's blade. After all the powder is added, the suspension is mixed for 4 h at 1500 (rpm). The final aspect of the base is a white/transparent liquid dispersion.

Before starting the suspension preparation, the base undergoes the process of sonication (Bandelin Sonoplus HD 2200) for 30 min; separated in 3 cycles to avoid overheating the equipment and the suspension. The actual amount of MS to be added must be corrected, because of material loss during the base preparation. It is known from theoretical values that the base is composed of 23.1% of NS and 76.9% wt of water, as can be calculated from reactions 1, 2 and 3:

$$\text{Base} = \text{HDK S13 (g)} + \text{H}_2\text{O} \qquad (1)$$

$$\text{HDK S13 (\%)} = \frac{\text{HDK S13}}{\text{Base}} \qquad (2)$$

$$\text{H}_2\text{O(\%)} = \frac{\text{H}_2\text{O}}{\text{Base}} \qquad (3)$$

Having the percentages, the quantity of MS can be corrected accordingly to the equivalent water. Although the final base's mass is not the same as measured, the percentages are, and can easily be compensated. To do so, the final base is massed and the quantity of nanopowder and water is obtained.

The process of adding the MS is the same as the conducted in the base preparation, being added gradually, with the mixer on and low rotation speed. After all the powder is added the mixer is set at a speed of 1500 rpm for 3 h.

The slip casting procedure is carried out by pouring the suspension into gypsum molds which are then put to dry inside an electric oven (Heraeus VT 6025), for ~24 h at 60 °C. After the pieces are dried, they are demolded and polished with sandpaper, to remove any possible gypsum contamination and then sintered accordingly to the sintering procedure, described in following topics.

3.2.1.2. 3D-Printing

Similar to the slip casting technique, robocasting needs a suspension-like material, which is called suspension. The suspension preparation differs from the previous one mainly because of the rheology needed to be printable and maintain the form without the assistance of any kind of solid support, such as molds. For this method, the suspension requires a previous powder preparation.

The powder preparation consists of adding step by step 9 wt.% of silica nanopowder (NS) into ethyl alcohol 70° containing 1 wt.% of dispersant (Duramax D-3005). The idea of adding Duramax is based on the previously explained principle of electrostatic stabilization, in order to achieve a resulting null suspension charge. The homogenization was performed in a laboratory mixer (RW 20 S32, IKA® Works Inc., USA) at 300 rpm, using a dispersing tool, until all nanopowder has been incorporated. Afterwards, MS powder was stepwise added to this previous NS mixture to complete up to 70% solids.

After complete mixing, the suspension was wet-milled for 3 h at 350 rpm using a high-energy planetary mill (PM100 Retsch), with high-alumina grinding media. It is followed by a complete solvent removal for 24 h inside a muffle oven at 100 °C. To finish, the dried material was sieved through a 45μm screen (#325 Mesh), in order to obtain the nanosilica-coated microsilica (NMS) powder.

The objective of this procedure is to obtain a homogeneous suspension combining both particle sizes, so that a higher stability is achieved when compared to the single suspensions. The idea is to obtain an optimized microstructure, where the nanoparticles are attached to the surface of the microparticle. By obtaining this nanosilica-coated microsilica (NMS) particles, the goal is to keep the powder in a stable state over time, in the sense that it can be used to prepare the suspension and still remain deagglomerated.

With the raw material prepared, Figure 15 shows the simplified flowchart for the 3D printing process.

Figure 15 - Simplified 3D printing flowchart.

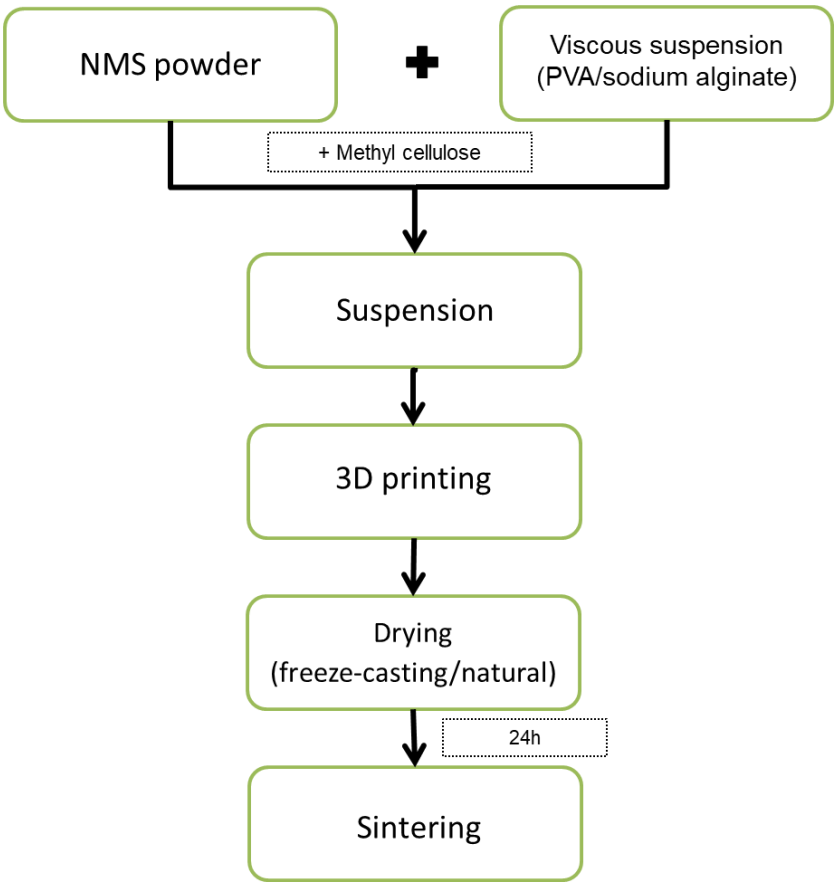

After having the NMS powder, the suspension can then be prepared by adding the desired quantity of solids into the viscous suspension. The final solid: liquid ratio can be calculated by using equations 4 to 6.

$$\text{Total (g)}_{\text{suspension}} = \text{Powder (g)} + \text{Gel (g)} \qquad (4)$$

$$\%\text{Solids}_{\text{suspension}}.\text{Total (g)}_{\text{suspension}} = \text{Powder (g)} + \%\ \text{solids}_{\text{gel}}.\text{Total (g)}_{\text{gel}} \qquad (5)$$

Combining (4) and (5), the following equation can be obtained:

$$\%\text{Solids}_{\text{suspension}}.(\text{Powder (g)} + \text{Gel (g)}) = \text{Powder (g)} + \%\ \text{solids}_{\text{gel}}.\text{Total (g)}_{\text{gel}} \quad (6)$$

The idea is to input the desired amount of solids in the suspension as well as the quantity of powder to be used and from that calculate the quantity of gel that should be added to the powder in order to obtain the expected concentration. The powder moisture is disregarded and the percentage of solids content in the gel is stipulated according to the preparation described before. With such information and the data from Equation 6, the suspension composition is determined.

The suspension is prepared by adding, step by step, the powder into the gel suspension, while stirring at 1200 rpm. The final rheological aspect of the suspension should be liquid enough that

it can be deposited by applying pressure and solid enough to maintain a filament form after printed. If needed, a thickener can be added. In this case, methyl cellulose is eventually used, and the solids content disregarded, as the additives are removed from the final printed parts in the sintering process. The thickener is added into the gel and mixed, before adding the powder.

The printing step of the 3D printing can be divided into three steps: pre-processing, machine printing and after-processing. The first one consists of developing the desired 3D model in a drawing software, followed by its conversion into the adequate format (from .cad to .stl). [44] The second one is the actual printing. The model is downloaded to the printer and the machine starts working on constructing the 3D sample. To conclude, after-processing and characterization are the steps in which the samples are done and may require a differentiated removal prom the 3D printer table, a specific drying procedure or another after-printing process to enhance the material properties (sintering, superficial treatments, coatings). [26]

The principle of the 3D-printing technique is the extrusion of a continuous filament, which must present a viscoelastic behavior, having its viscosity reduced with the increasing shear tension, in order to have a controlled flow through the extrusion nozzle and to be able to maintain form after being deposited over the printer table of the previous layer. [45]

The 3D printer used (DuraPrinter E01), Figure 16, is based on the Direct Inkjet Writing (DIW) technique to produce three dimensional models. This printer has a static table, which works as the solids support. The geometry of the samples is printed according to the synchronized movement of three motors, which allow the head to freely move in the X, Y and Z axis. [46]

Figure 16 – Photography showing the 3D printer (Duraprinter E01) used in this work.

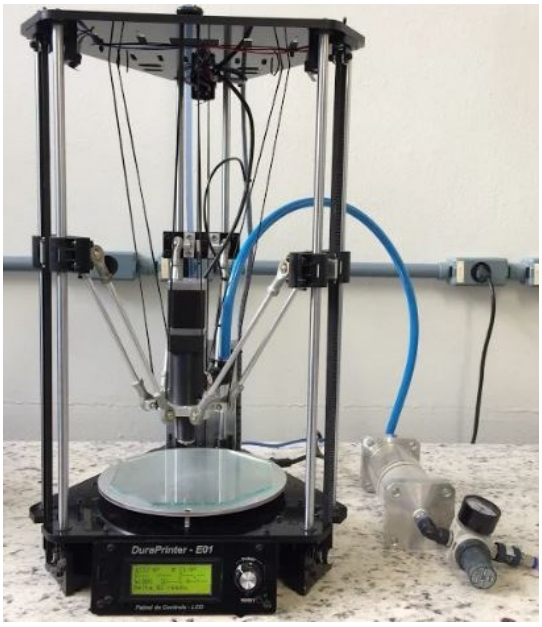

After the manufacturing process, the samples were dried inside a controlled humidity chamber for a period of 24 h, followed by the sintering. The sintered parts were not polished due to the complex forms that would be compromised by the mechanical procedure.

Having the parts printed, the drying requires careful attention, as in this part of the process cracks can happen due to the water evaporation. In order to have some control, two different drying paths were chosen: room temperature inside a controlled humidity chamber or freeze drying. As The second technique consists of freezing a liquid suspension (aqueous or not), at – 42 ºC for 3 hours followed by sublimation of the solidified phase from the solid to the gas state under reduced pressure (vacuum of 100 mbar) at – 42 ºC for the period of 24 hours, and subsequent sintering to consolidate and densify the walls, leading to a porous structure with unidirectional channels in the case of unidirectional freezing, where pores are a replica of the solvent crystals. This process can turn the presence of pores inside the material from an unwanted result into an interesting feature to be explored and increase the range of applications [47].

For a 3D printing process, the suspension needs to present a few key characteristics, such as be fluid enough to be deposited through the nozzle and viscous enough to support itself and the following layers. The sodium alginate-based suspension was prepared with 50% NMS powder to sodium alginate ratio. As a thickener, 0.75 % of the solids content of methyl cellulose was added. The PVA suspension was prepared in a 65% NMS powder to 35% PVA ratio, with the addition of 1% methyl cellulose. The concentrations of the suspensions were obtained from a series of tests, from which the unsuccessful suspensions did not even present the adequate behavior to 3D print. The 3D printer was fitted with a reservoir (syringe) and a nozzle with 1.11 mm diameter nozzle. The starting parameters were set at 1.6mbar bar pressure and 10 mm/s printing speed for both suspensions. During the process, changes were performed to maintain the suspension deposition flow constant and straight, avoiding the deposition of clusters or depressions.

3.2.2. Firing

For slip-cast parts vacuum sintering of 0.30 mbar in a Nabertherm RHTC 80-450 furnace was used to provide a clean atmosphere without the contact with air, which can cause grain growth, consequent crystallization and possibly evaporate impurities from the high surface of the material. [48]

The firing parameters used for the slip casting procedure can be seen in Table 8 and were stipulated based on previous work by Jerman [19]. It is important to notice the temperatures in which there are steps, because they are determined in order to prevent crystal formation and lower the possibility of cracks that could induce crystallization.

Table 8 - Sintering parameters for slip-cast parts.

Parameter (Unit)	Value
t (°C/min)	5
T0 (°C)	25
T1 (°C)	120
Hold 1 (min)	120
T2 (°C)	350
Hold 2 (min)	60
T3 (°C)	1250
Hold 3 (min)	240
T4 (°C)	1500
Hold 4 (min)	60
Vacuum (mbar)	0.30

The step is set at 5 °C/min to avoid any fast heating that could induce cracks. The vacuum is also used as it can reduce grain growth and also induce cracks or the formation of crystalline forms. The first step at 120 °C is to allow the water to evaporate, followed by 350 °C in which the phase transition of amorphous silica into α-quartz may occur. At 1250 °C, it can turn into β-cristobalite and at 1500 °C is delimited as the sintering temperature.

For the additive manufactured parts, a conventional atmosphere sintering was applied. The biggest difference between the two processes is that slip-cast parts needed a complete inert and impurity-free environment in order to maintain the amorphous form of the powders and, consequently, obtain transparent and crack-free parts. Due to the presence of additives and applications of the 3D printed parts, the crystallization process is no longer an issue and can be used as a benefit, expanding the possible applications of the final printed parts.

The 3D printed parts sintering parameters can be found in Table 9.

Table 9 - Sintering parameters for 3D-printed parts.

Parameter (Unit)	Value
t (°C/min)	5
T0 (°C)	25
T1 (°C)	650
Hold 1 (min)	120
T2 (°C)	1200
Hold 2 (min)	120
T3 (°C)	25

The step is maintained at 5 ºC/min; however, the holding temperatures chosen are different than those compared to the slip casting procedure mainly because of the presence of additives in the first one. The T1 is no longer as low as 120 °C because the water is presented as the sodium alginate gel. Dispersant and binder are removed at around 600 °C, so the T1 is set at around 10% higher, 650 °C. The highest sintering temperature goes up to 1200 °C due to furnace restrictions.

3.2.3. Characterization

The aim to characterize is to further understand both the material structure and behavior. Based on the materials description, this topic is also separated in three major categories: powder, suspension and parts (green and sintered parts). The goal is to be able to understand the process as a whole, from the raw materials up to the final parts.

3.2.3.1. Particle Size Distribution

To characterize the solid material utilized, two different techniques were utilized, due to the different size scale (nano – NS and micro - MS). The technique used to obtain microparticles size distribution was Laser Diffraction (LD, Malvern Mastersizer S). The sample was analyzed through a 0.01% volume suspension in isopropanol. Tests using a tip sonicator were conducted but no significant changes were noticeable. In order to obtain the particle size distribution of the nanopowder, Dynamic Light Scattering (DLS) was applied.

3.2.3.2. Stability and Rheology of Suspensions and Suspensions

The zeta potential (Malvern Zetasizer Nano ZS ZEN3600) measurements were conducted within a polycarbonate cell and a titulometer attached to the equipment, with pH ranging from 2 to 10.

The pH was adjusted by the addition of HCl or NaOH solutions. The electrophoretic mobility of the particles was automatically converted to the zeta potential value using the Smoluchowski equation by software (Zetasizer Nanoapplication 11). The suspensions were all prepared at 1 wt% aqueous suspension. The preparation consisted of adding the powder to water and mixing for 30 min at 800 rpm. All the prepared solutions went through an ultrasonic bath for 5 min before being put into the equipment.

Flow curves of suspensions and ceramic suspensions (printable suspensions) were evaluated using a rotational rheometer (Haake Viscotester iQ, Thermo Fischer Scientific, DE) with concentric cylinders (CC27/Ti) and parallel plates (P35/Ti; with a gap of 1.0 mm), respectively. Measurements were performed under steady-shear conditions by applying a stepwise stress increase until a shear rate of at least 1000 s^{-1} was reached (in 180 s).

3.2.3.3. Density and Porosity

The bulk density of slip cast transparent disks was measured according to the Archimedes method by ASTM C20-00 (2012), Equation 7. [49]

$$\rho_{bulk} = \frac{m_{dry}}{m_{dry} - m_{immerse}} \text{ x } \rho_{H2O} \qquad (7)$$

The masses are obtained experimentally, and the water density is found in the literature in a broad range of temperatures.

The density of powders was measured by the gas displacement method, according to ASTM B923, it is used for pore volume measurements through a helium pycnometer based on Boyle-Mariotte's law of volume-pressure relationships. [49] The method consists of placing a dry specimen of known bulk volume (V_{bulk}) in a container of known volume (V_a). This container is connected to another (V_b) that is evacuated. The inert gas is introduced into V_a and pressure (P_1) set to an arbitrary value, followed by the release into Vb, allowing to equilibrate between both chambers. The inert gas then penetrates inside the pores and the pressure will decrease to a new stable level (P2). Using the ideal gas law, the volume of pores (Vv) can be calculated through Equation 9: [49]

$$V_v = V_{bulk} - V_a - V_b \left(\frac{P_2}{P_2 - P_1}\right) \qquad (9)$$

The sample mass and the temperature are constant during the measurement. With the pore volume obtained, the picnometric density is calculated according to Equation 10:

$$\rho_{pure} = \frac{m}{V_v} \qquad (10)$$

To obtain the sample's porosity, the dimensions are measured with a caliper rule, the mass measured in a scale and the density calculated similarly to Equation 10, where the volume is

obtained from the part's geometrical form. At last, the percentage of porosity is obtained according to Equation 11:

$$\% \text{ Porosity} = \left(1 - \frac{\rho_{\text{calculated}}}{\rho_{pure}}\right) \text{x } 100 \qquad (11)$$

The true density of 3D-printed porous parts was measured using a picnometer (Quantachrome Ultrapyc 1200e). A green 3D printed part was crushed and sieved at #325, then set inside the equipment's powder holder. This technique was used to determine the true density of the nanosilica-coated microsilica (NMS) powder.

3.2.3.4. Structural and Microstructural Analysis

In this work, Transmission Electron Microscopy (TEM), Scanning Electron Microscopy (SEM), Field Emission Scanning Electron Microscopy (FESEM) and X-ray diffraction (XRD) were used.

For the morphological characterization of MS and NS powders, transmission electron microscopy (TEM) was chosen, given the possibility to further investigate the powders internal structure. The suspensions were prepared by adding a spatula tip of the corresponding powder into a falcon tube filled with isopropyl. The suspensions then went under an ultrasonic bath for 5 min (UltraCleaner USC 750 Unique and a droplet of each placed into a carbon-coated copper grid (CF400-Cu, Electron Microscopy Science Co), stored in a desiccator for 24 h prior to the TEM analysis. The analyses were performed using a microscope (JEOL JEM 2100), operated at 100 kV with a resolution of 0.27 nm.

Sintered SEM samples were prepared by slicing a small piece of the 3D parts and placing them in a copper stub, with a carbon tape. The equipment used was a Scanning Electron Microscope (SEM, Hitachi TM3030l), which operates with a 5 up to 15 kV and magnifications of 15 up to 30,000x.

Field Emission Scanning Electron Microscopy (FESEM) was applied to NMS powder to provide a clear and less distorted image when compared to regular SEM analysis. FESEM samples were prepared from the NMS powder suspension dispersed in isoprophyl alcohol by applying 5 min of ultrasonication (UltraCleaner USC 750 Unique). Then, a droplet of the suspension was deposited on a carbon tape in a copper stub at 50 ºC and dried for 12 h. The sample was covered with a gold layer, since the material is nonconductive. The equipment (FESEM, JEOL JSM-6701F) has an emission source of LaB6 and resolution of 1nm. In addition, a qualitative elemental analysis (chemical composition) was performed on different microscopic sections of the sample by energy dispersive spectroscopy (EDS), coupled at a FESEM. In other words, the chemical composition of the material can be estimated in percentage. For the elemental analysis, the optimum resolution of the scanning images (related to beam diameter) is from 0.1 to 1 μm. [50]

The crystallographic structure of the as prepared NMS powder, sintered 3D-printed filament powder, and sintered disks, was determined by X-ray diffractometry, (Rigaku MiniFlex600 DRX - with Cu Kα, 40 kV, 40 mA, 0.01°, 2s). The XRD patterns were analyzed using the X'pert HighScore Plus package program, and the crystalline phases were identified according to the JCPDS database. In addition, the relative percentage of the crystalline phases present in each sample was determined by Rietveld refinement [51]

3.2.3.5. Thermal Analysis

DTA was performed for silica powders in a thermal analyzer (Netzsch STA 409 C/CD) using an alumina crucible , with an inert air flow (100 mL/min), the temperature set to increase up to 1600 ˚C under a heating rate of 10 ºC/min and a weighted mass of approximately 30 mg. The thermal analysis was performed in order to evaluate if the pre-established firing parameters are sufficient for the thermal treatment desired.

Dilatometric analyses were conducted with the 3D printable suspensions (NMS + sodium alginate gel and NMS + PVA gel). The idea of dilatometry is to observe changes in the dimensions of the specimen while it goes under a heating process. The linear shrinkage of the materials was obtained using an optical dilatometer (Expert System Solution Misura ODHT), at a heating rate of 10 ºC/min, in the temperature range of 25 to 1200 ºC, and static natural air.

3.2.3.6. Optical Properties

For the quantification of optical factors, a spectrophotometer UV-vis is used. In this equipment, two variables to measure transparency were obtained: opacity (%) and the material translucency index (TP).

Opacity is an important attribute of appearance, especially over diffuse media that speculate. The term is used to indicate numerically the capacity of a surface (material) to cover or hide the surface below or behind it. Its determination is important for suspensions, papers, films, plastics and other paper Opacity, for example, is the property of the paper that minimizes the perception of printing through the sheet, printing the back of the page or the next sheet. Opacity is usually expressed in terms of contrast ratio; it is the ratio of the reflectance factor obtained from measuring color over contrast (white and black). [52] It is obtained directly from the equipment, calculated according to Equation 12:

$$\%\ \text{Opacity} = \frac{Y_{\text{black}}}{Y_{\text{white}}} \qquad (12)$$

where:

Y is the luminosity tristimulus, and the values of opacity range from 0 to 100%.

The other parameter evaluated was the translucency, which can be understood as the relative amount of passage of light through an object. When the material is absolutely turbid (opaque), translucency is zero. Consequently, the higher the TP value, the greater translucency of a material [53]. The measurement is given through the Translucency Index (TP), which is obtained with the parameters L*a*b from the Commission Internationale de l'Eclairage (CIELab) system. It is defined as the color difference between black and white backgrounds with equal thickness and matches with the visual translucency evaluation. The L* parameter indicates luminosity and it ranges from 0 (indicates black) up to 100 (diffuse white). As for the a* it is the coordinate between green (-60) and red (+60). As for b*, it represents blue (-60) and yellow (+60). Using this coordinate system, an object`s color and transparency can be obtained and quantified, instead of just analyzed visually. [54] . Such technique is important for materials that must maintain a color or transparency pattern. With these variables, the Translucency Index can be calculated according to Equation 13.

$$TP = \sqrt{[(L*_b - L*_w)^2 + (a*_b - a*_w)^2 + (b*_b - b*_w)^2]} \qquad (13)$$

For TP, the higher the value, the more translucent the material.

For optical characterization, the sintered parts were polished (Struers TegraForce-5) using three different diamond disks with particles ranging from 9, down to 3 and then 1 μm and a diamond suspension with the same corresponding particles` size , to remove the surface roughness, which can be understood as a surface formation of crystalline polymorphs of silica.

Extremely important characterization for the slip-cast parts, are the optical features. These properties may influence how effective the transparency or translucency of the objects are and consequently their range of applications. As mentioned before, % opacity and translucency index (TP) were obtained using a spectrophotometer (Konica Minolta CM 3600A). For this quantification two slip-cast disks, Disk 1 with a 23.10 mm diameter; 4.50 mm thickness and Disk 2 (right) with a 23.01 mm diameter; 4.52 mm thickness, were measured for comparison As for the light emission, three sources were used: D65/10º, A/10º and CWF/10º.

4. RESULTS AND DISCUSSION

4.1. Characterization of Silica Powders

4.1.1. Particle Size Distribution

As specified by the microsilica manufacturer, the size range should be in the micrometric scale and is confirmed by the analysis, which can be seen by the volumetric distribution and the D50, expressed in Figure 17.

Figure 17 - Particle size distribution of microsilica (MS).

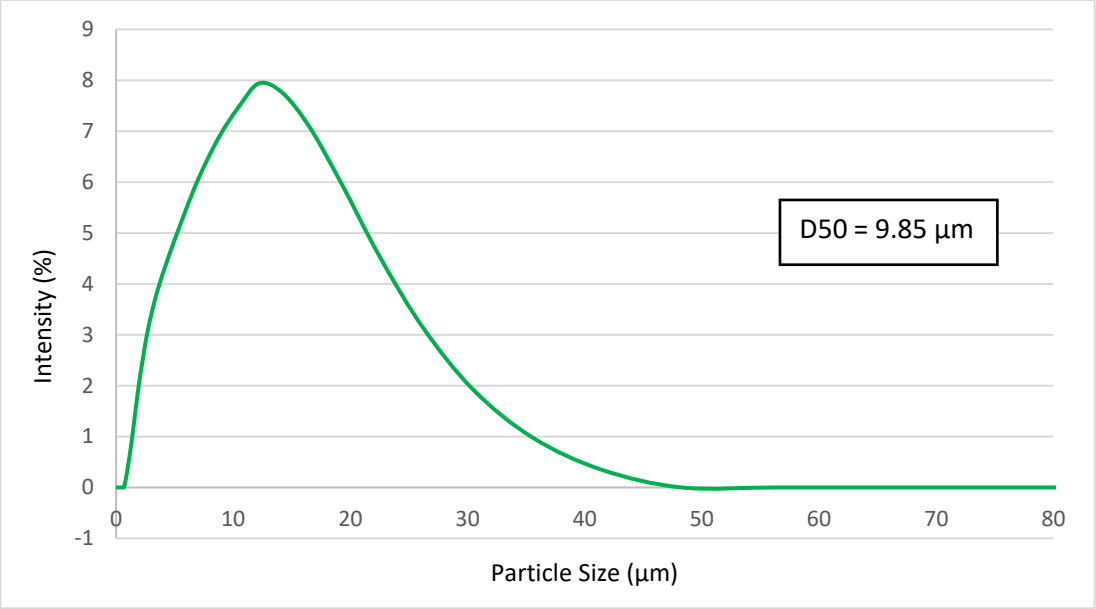

As it can be understood, the particle size ranges to nearly 50 µm. This can be seen by the large base of the graphic and can be related to the tendency of the particles to agglomerate or not. A further understanding of such behavior is explored in the analysis of stability and morphology.

Using the same technique, the NMS was characterized after diluting the powder into a 1% wt suspension, followed by a 5 min ultrasonic bath. The particle size distribution as well as the D50 can be seen in Figure 18:

Figure 18 - Particle size distribution of nanosilica-coated microsilica (NMS).

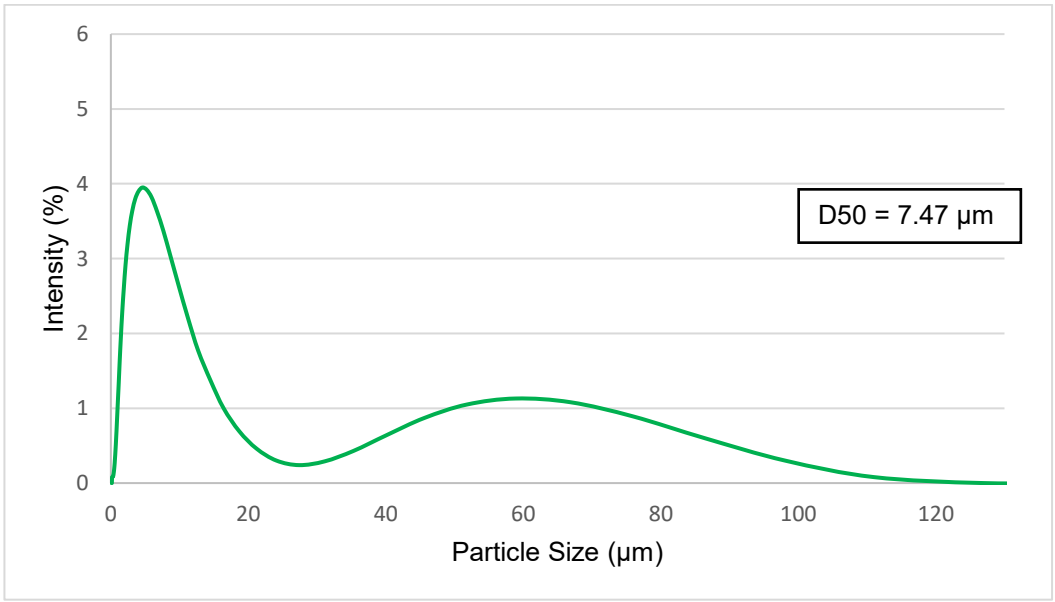

After a careful evaluation of the data, it is possible to see that the size distribution ranges to over 1000 µm. This is possible due to the presence of possible residual nanopowder that did not link to the micropowder and the formation of agglomerates, which can be seen from the large base of the graph. Looking at the d50, it is possible to have an idea that although there is a higher presence of bigger particles, the size is similar to the MS powder. Evaluating these results together with zeta potential (-37.7 mV) it is possible to say the powder has a large variation in size, but it is not due to the lack of stability, but instead of the processing technique, that does not predict a size range in which the final NMS should be within.

For the nanopowder characterization, DLS was applied to a 1% wt solid aqueous water suspension. A tip sonicator was used for 2 min to provide possible agglomeration of the powder and the results can be seen in Figure 19. The base represents the range from which the size present in the suspension range, and, from the graphic, can be seen that it goes from around 100 nm up to nearly 800 nm. Such variation can be related to the natural powder behavior to agglomerate, which is not ideal for the stability of the process. The addition of surfactants can be considered if the agglomeration is too severe and can alter the final results. For this case, the natural tendency is not as significant, and the expected results are obtainable without the need the addition of any kind of stabilizers.

Figure 19 - Particle size distribution of nanosilica (NS) powder.

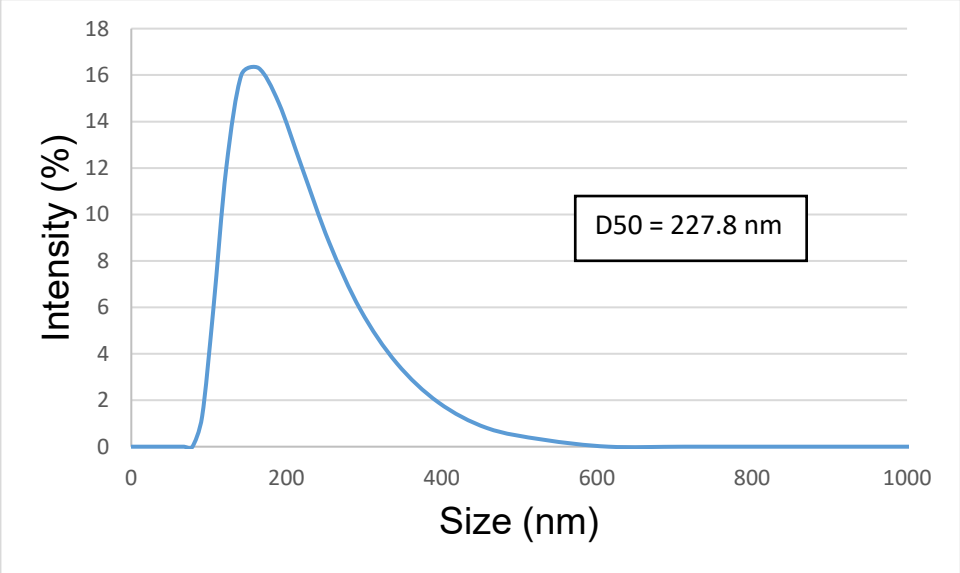

4.1.2. Powder Microstructures

Figure 20 shows the TEM images obtained for the MS particles, with a scale of 100 and 50 nm, and magnifications of 150.000x and 300.000x, respectively. At high magnification images, MS particles feature mainly irregular particle aggregates in the range of 150 nm.

Figure 20 - TEM images of microsilica (MS) powder, in which (a) represents a scale of 100 nm and 150.000x magnification; (b) 50 nm scale and 300.000x magnification.

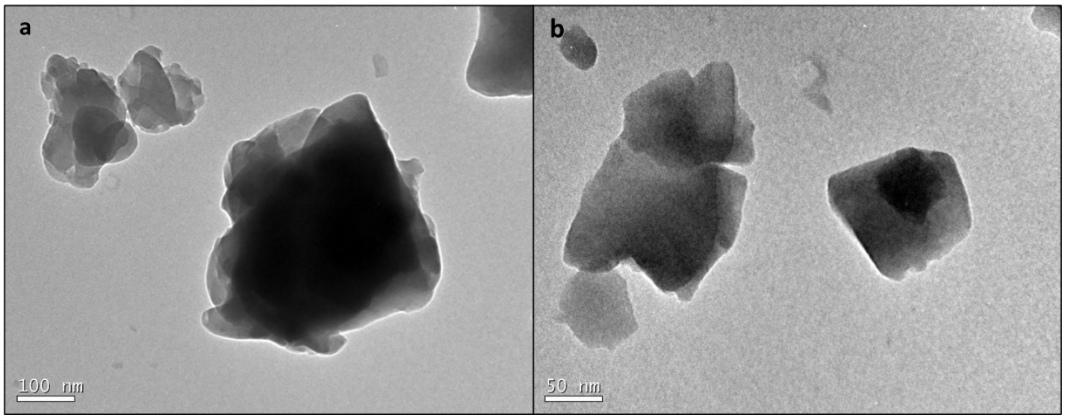

It is possible to observe in the images that the particles are, as the manufacturer stated, in the sub-micrometric scale. The contrast between the light background and the dark particles is enhanced by the fact that there is probably the formation of agglomerates and the fact that they overlap, providing the impression of a densely packed material. In a more profound investigation, related to the particle's size, the smaller it is, higher its surface energy associated with the creation of new surface, and consequently, the particle became more reactive, i.e., the contact between adjacent particle is improved, which can influence the homogeneity, porosity, sintering (that starts at lower temperatures), and consequently directly impact the final mechanical properties of fired ceramics. [55]

As for the NS analysis, the images can be seen in Figure 21, with 100 and 50 nm scale, and 120.000x and 400.000x magnification, respectively. A typical three-dimensional array of nanoparticles in the range of 20 nm is observed.

Figure 21 - TEM images of nanosilica (NS) powder, in which (a) represents 100 nm scale and 120.000x magnification and (b) 50 nm scale with 400.000x magnification.

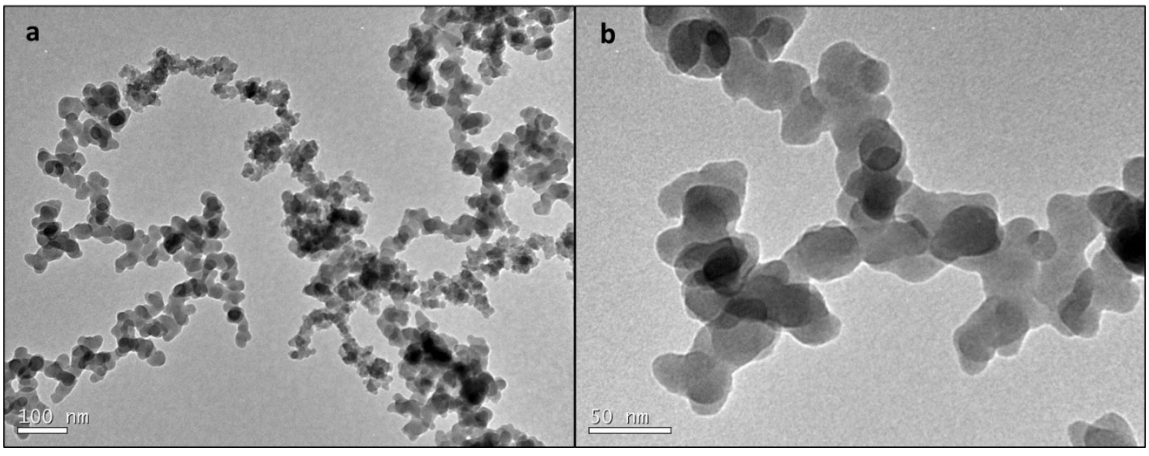

To ensure a complete characterization of the material size, imaging techniques, such as TEM, should be evaluated together with size distribution techniques, like DLS. As previously mentioned, the average particle size measured was of around 227 nm. Through a careful analysis of TEM images, it is possible to see that there are particles smaller than 50 nm. This diversion in the two results can be understood through a closer look at the microscope pictures. Although they are smaller when looked individually, such state is not achieved in the working conditions, as they are connected, like a chain, forming agglomerates, which backs up the results of DLS. It is also important to remember that TEM analyzes part of the suspension, while DLS gathers the result from a distribution.

The morphological aspects of the nanosilica-coated microsilica (NMS) are shown in Figure 22. It can be seen from FESEM images, using 15,000×, 10,000× and 5,000× magnifications, respectively.

Figure 22 - FESEM images of nanosilica-coated microsilica (NMS) powder.

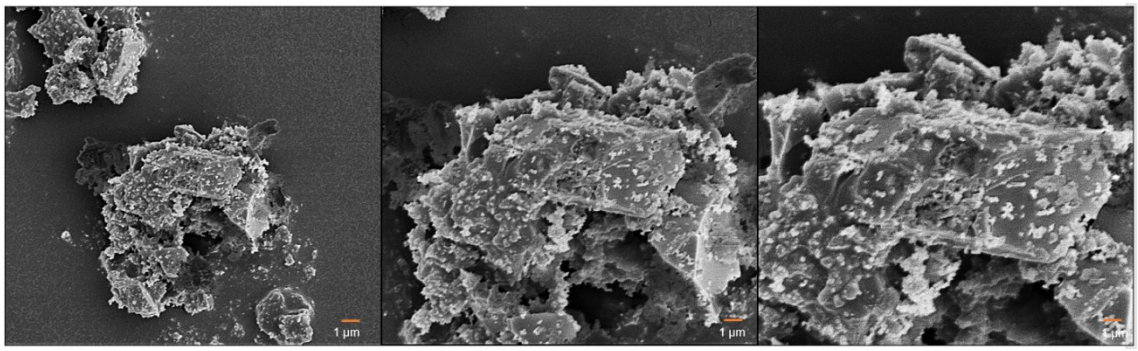

FESEM images (Figure 22) were taken to confirm if the preparation of the NMS powder was successful. From the image, the nanoparticles are indeed attached to the microparticles. The hypothesis for such material formation is that both powders, as previously observed, tend to agglomerate. By incorporating the nano onto a microparticle directly, instead of preparing one then adding the other, induces the agglomeration between different sizes. Also, because the MS is much larger than the NS, when the smaller particles are looking to attach, they tend to find first the larger, consequently forming the NMS as observed. As previously mentioned, the stabilization of suspension can be achieved mainly through three methods: steric, electrostatic and electrosteric. Due to the surfactant used (Duramax D-3005) being a polyelectrolyte salt with features to act as an electrostatic stabilizer, the surface charges between particles tend to the neutral and consequently providing the possibility of attachment from the NS into the NMS.

As previously said, together with FESEM, an EDS is conducted to chemically characterize the material. To do so, a small part of the 15,000× image was scanned, and the results obtained are expressed in Figure 23.

Figure 23 – Chemical composition (EDS) of nanosilica-coated microsilica (NMS) powder.

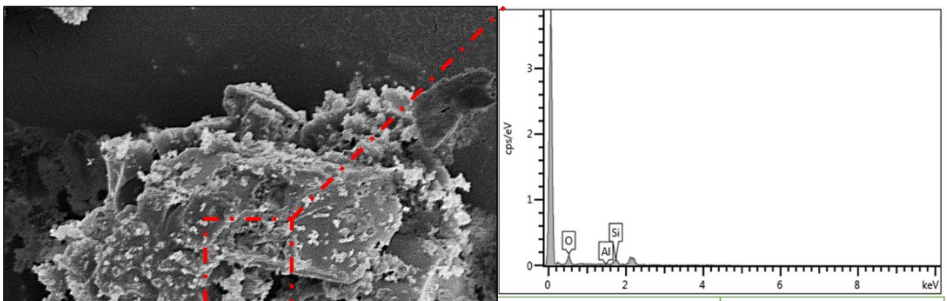

Element	Wt (%)
Si	49.16
O	49.32
Al	1.52

It is possible to visualize that the middle of the sample was selected, to exclude any possible interference from the background material. The sample should be comprised of only silicon and oxygen (SiO_2), but the presence of aluminum is not unexpected. As previously explained in the suspension preparation, the vessel that goes into the high energy mill is filled with high-alumina balls to increase the milling. It is possible that because of the suspension impact with the milling balls, some residual contamination happened, which was carried with the powder all the way through the whole process.

4.1.3. Stability and Rheology of Suspensions

As mentioned before, an important parameter to evaluate stability of a suspension over time, is the zeta potential. The characterization was performed for the nanopowder (NS), micropowder (MS), and the coated powder (NMS). The idea is that when the zeta potential is higher than ± 30 mV, the suspension is stabilized. It is important to notice that the zeta potential alters as the pH of a suspension changes as well as the concentration that the suspension is prepared. As the analyses were performed in order to better understand the behavior of the powders, and the pH was not changed for the suspension and suspension preparations. The pH was still measured separately to identify which is the actual state that the material is. Firstly, the data regarding the NS powder is expressed in Figure 24. The pH at 25 ºC is of 6.90.

Figure 24 - Zeta potential of nanosilica (NS) powder.

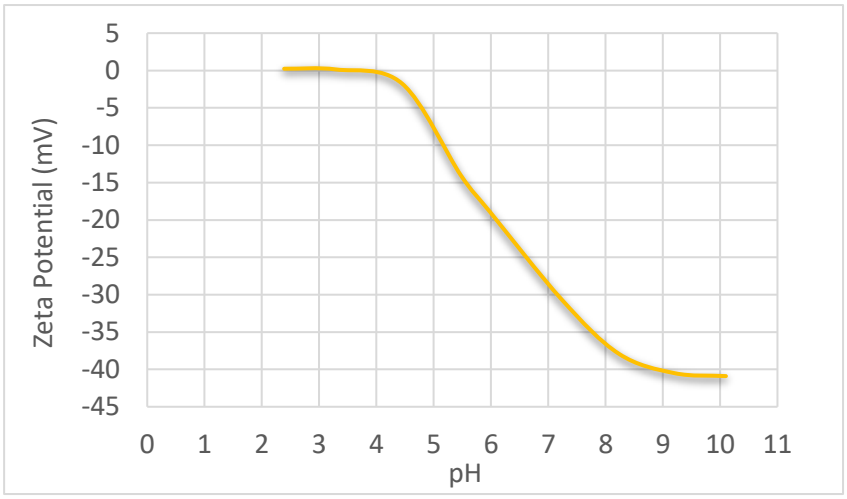

The nanopowder crosses the IEP at the pH of 3.38, as measured by the equipment. It is possible to see that as the suspension`s pH increases toward basic, the more stable it is, presenting a negative zeta potential. At the working pH of 7, the value is of approximately -30 mV. It can be said that, at the normal state, the suspension is stable.

For MS, the results are shown in Figure 25. The initial pH at 25 ºC was similar to the nanopowder: 6.47.

Figure 25 - Zeta potential of microsilica powder (MS).

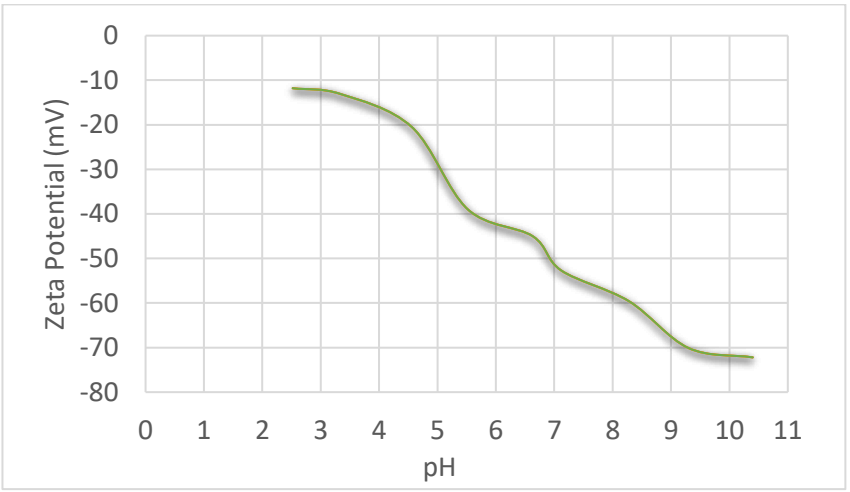

The information gathered in the MS zeta potential graph shows that it is more stable than the NS. Ranging from 2 to 10, the most unstable measurement was at the most acid conditions, reaching around -10 mV. The same behavior could be seen, as the pH was raised. At the pH of 7, the zeta potential was approximately -50 mV.

Regarding the NMS, the information is shown in Figure 26. The pH at 25 ºC was of 5.34, a little lower than to the two powders separately.

Figure 26 - Zeta potential nanosilica-coated microsilica (NMS) powder.

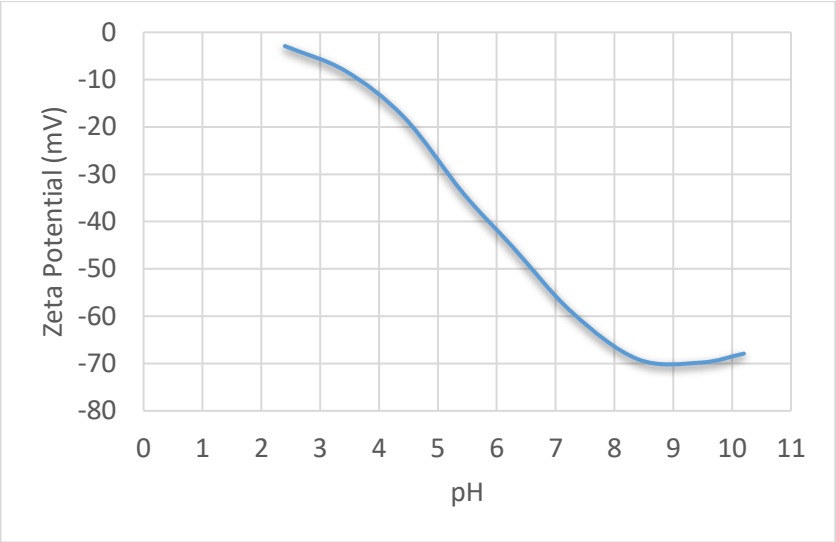

At more acid pH, the suspension tended to destabilize and at the more basic range, to be more stable. At the working pH of 5.34, the measured zeta potential was approximately of -35 mV. As previously explained, values above ± 30 mV can be roughly considered stable and so, the NMS.

A final graphic was constructed with the results of all three measurements, in order to evaluate the behavior of each powder, as can be seen in Figure 27.

Figure 27 - Zeta potential of silica suspensions compared: NS, MS, NMS.

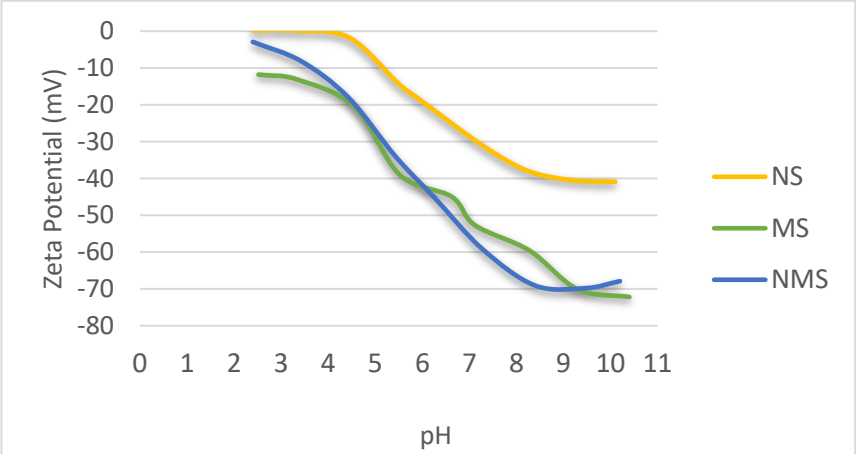

Firstly, the nanopowder in all pH extension presented with a higher zeta potential to the other two, which can be attributed to the fact that nanoparticles tend to be less stable than bigger sized particles. A peculiarity is seen between the MS and the NMS, as they present a rather similar behavior with some shifts along the pH, in points such as the pHs of 4.5 and 6.5, approximately.

A conclusion that can be taken from this comparison is that, as the NMS is produced from the other two specimens, the micropowder behavior is more significant than the nanopowder, as it is to be expected due to the size comparison of about 5 times bigger, as previously shown.

In order to obtain well-dispersed microsilica (MS) powder suspensions, suitable for slip casting processing route, the influence of different concentrations of nanosilica (NS) powder on the viscosity of the suspensions was investigated. Flow curves for the MS suspension containing 9 wt.% of NS are reported in Figure 28. It is interesting to note that the microsilica suspensions exhibit a non-Newtonian, characterized by a pseudo-plastic behavior (shear-thinning), i.e., the viscosity decreases with the increase of shear rate (blue curve). In addition, significant differences between up and down curves (hysteresis), as a function of both shear rate and time became evident, as a result of a build-up colloidal structure formation or thixotropy (black curve). [56] [57]

According to Moreno (2005), a possible explanation for their pseudo-plastic behavior is that, under shear, the irregular-shape particles trend to be aligned with the flow, broken the agglomerates structure formed. [57]

Figure 28 - Flow curves of 61 wt. % microsilica (MS) powder suspensions containing 9 wt.% of nanosilica (NS) and 30 wt. % of water.

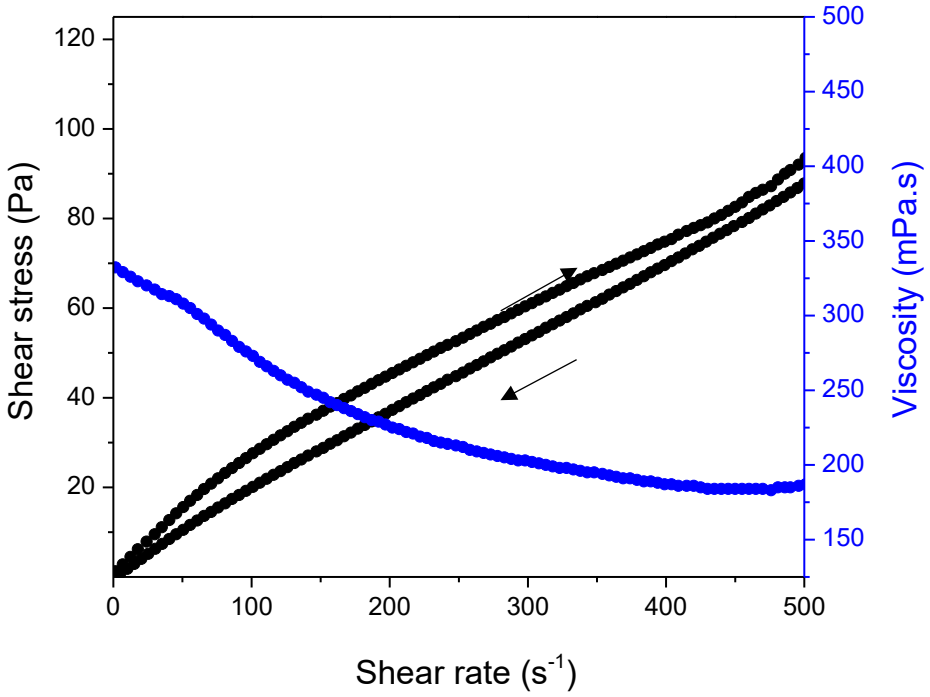

Figure 29 shows flow curves for the MS suspension containing 12 wt.% of NS. It can be seen a similar pseudo-plastic behavior and thixotropy. It is possible to observe the increase in viscosity when a greater concentration of NS is present in the suspension. Maintaining the solid: liquid ratio, the decrease in particle size leads to a higher number of particles present in the suspension,

which consequently results in a significantly higher in the surface area. The higher values of viscosity are a result to the combination of a bigger number of particle's present and the resulting collision between them. [56] [57] [58]

Figure 29 - Flow curves of 58 wt. % microsilica (MS) powder suspensions containing 12 wt.% of nanosilica (NS) and 30 wt. % of water.

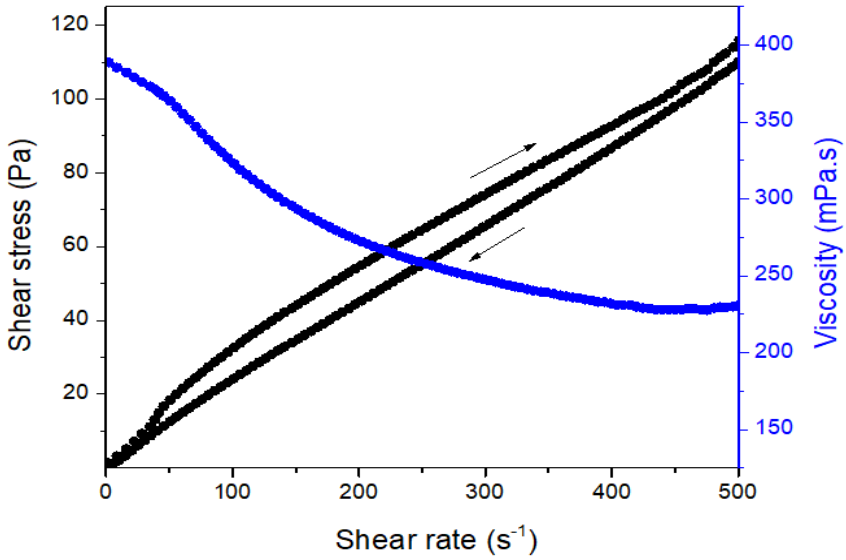

In 3D-printing process, the rheological properties of highly concentrated colloidal suspensions or suspensions determine the flow behavior during printing, as well as shape retention of 3D-structure thereafter extrusion, which will influence the final mechanical and/or functional properties [57] [4]. Thus, the viscosity as a function of shear rate curve of NMS alginate-based suspension with a ratio of 50:50 % wt was evaluated (Figure 30). Note that the suspension exhibits a shear-thinning behavior that facilitates filament deposition through the extrusion. [4]

Figure 30 - Viscosity as a function of shear rate curve of nanosilica-coated-microsilica (NMS) alginate-based suspension.

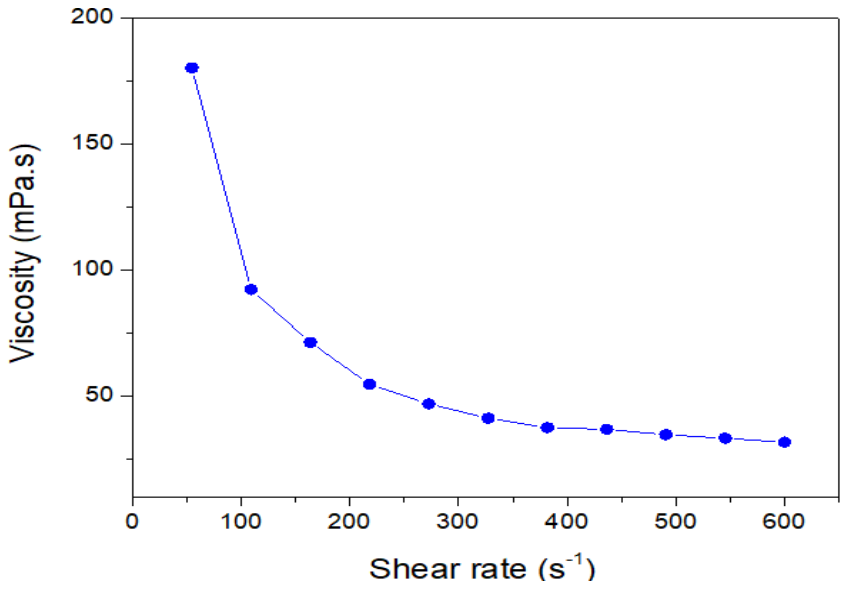

The shear stress as a function of shear rate curve of nanosilica-coated-microsilica (NMS) alginate-based suspension was also evaluated (Figure 31). Observe that the shear stress linearly increases approximately up to 10 Pa, which is equivalent to applying pressure region 1 on 3D printing, corresponding to an elastic deformation of the alginate-based gel network, then it approaches a plateau, equivalent to yielding extrusion region 2, corresponding to breakdown of the colloidal structure at 50 s^{-1} [57]. This maximum in shear stress indicates the presence of elasticity of the colloidal alginate-based gel up to the point of yielding. The overshoot before reaching a steady state value represents the transition of elastic properties and restructuring of the gel to a dynamic equilibrium. [56]

In addition, colloidal suspensions should flow at low applied stress or high velocity, since the yield stress cannot exceed the maximum pressure available in the 3D-printing system. [4]

Figure 31 - Shear stress as a function of shear rate curve of nanosilica-coated-microsilica (NMS) alginate-based suspension staggered curve.

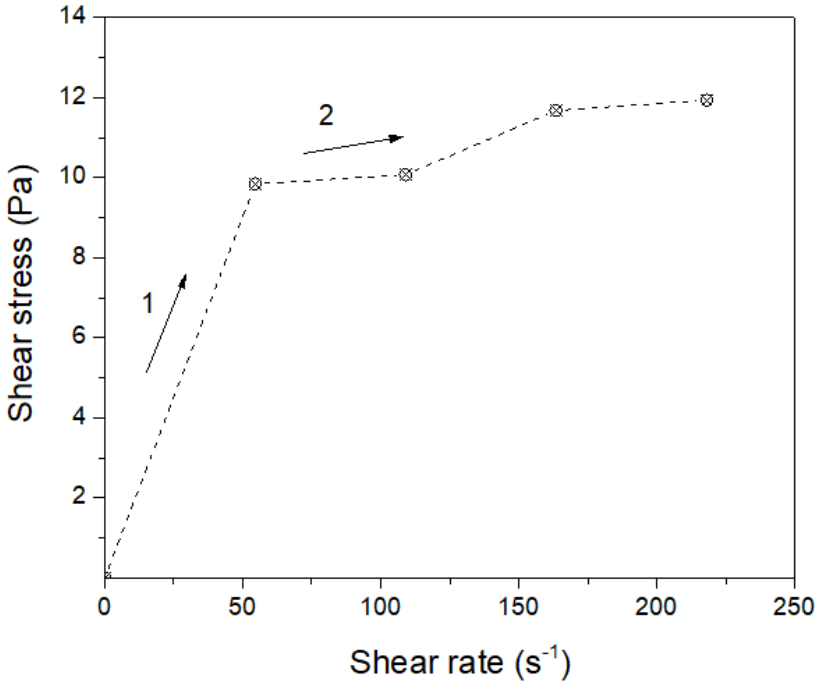

Based on the same concept of sodium alginate, PVA was used to produce a different suspension and evaluate the results and applicability with the NMS powder. The suspension formulation consisted of roughly 65% of NMS powder and 35% of PVA. Figure 32 shows the viscosity as a function of shear rate and its possible to observe that the shear-thinning behavior is still present, and the viscosity is significantly increased. Low viscosity enables the suspension deposition to flow more efficiently, though it spreads and collapsed. On the other hand, with high viscosity the

material can retain the shape, but to do so, higher pressure is necessary to dispense. For the successful printing process, high viscosity is desirable at low shear rates and low viscosity at high shear rates. [59] This behavior is clearly and more significantly seen when using PVA based suspension when in comparison to alginate based.

Figure 32 - Viscosity as a function of shear rate curve of nanosilica-coated-microsilica (NMS)/ PVA suspension.

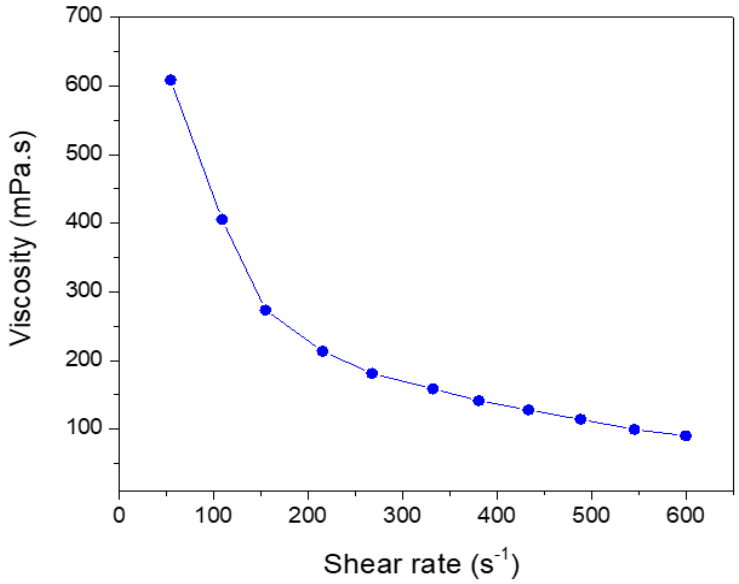

Following the procedure, shear stress as a function of shear rate of the PVA-based NMS suspension was analyzed (Figure 33). The initial linearity is still observed, but over 3 times bigger, reaching almost 35 Pa (region 1). This first jump is related to the pressure applied to the suspension inside the reservoir, reaching the region 2, or the yielding extrusion. The same overshooting behavior is observed in the PVA suspension corresponding to the transition of elastic properties towards dynamic equilibrium. [56]

Figure 33 - Shear stress as a function of shear rate curve of nanosilica-coated-microsilica (NMS) PVA-based suspension staggered curve.

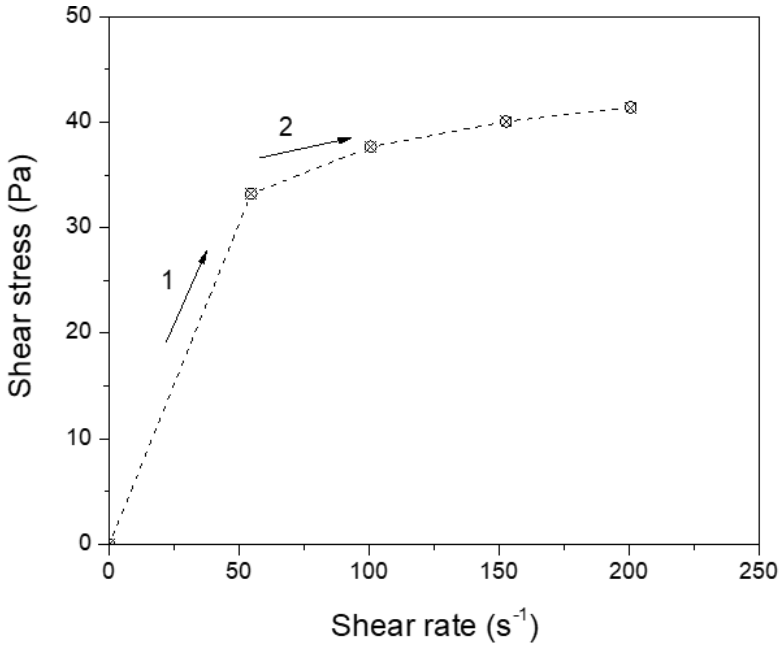

4.1.4. Thermal Analysis of Powders

Thermal characterizations were conducted for silica powders as well as for both slip-cast and 3D-printed parts. The idea of further investigating the thermal behavior is due fact that thermodynamically amorphous silica is unstable, as it can be devitrified due to the possibility of transformation from the amorphous structure to another crystalline phase during the manufacturing or firing processes, or when used at high temperatures. [7]

In the slip-cast parts, the amorphous state of the raw-materials must be preserved, otherwise the densification during sintering will not occur as expected and consequently crystalline parts may form, and the transparency won't be achieved. Regarding the 3D-printed parts, the thermal evaluation is important to evaluate which silicon dioxide polymorphs are present in the internal final structure of the parts, as they present different properties, organization and may affect the applicability.

The DTA and TGA analyses were conducted for the MS, NS and NMS powders. PVA and sodium alginate-based suspension filaments were analyzed by dilatometry. For the MS, the mass loss results can be found in Figure 34.

Figure 34 - TGA of microsilica (MS) powder with a synthetic air flow rate of 100 mL/min and a heat rate of 5 °C/min from 0 up to 1600 °C.

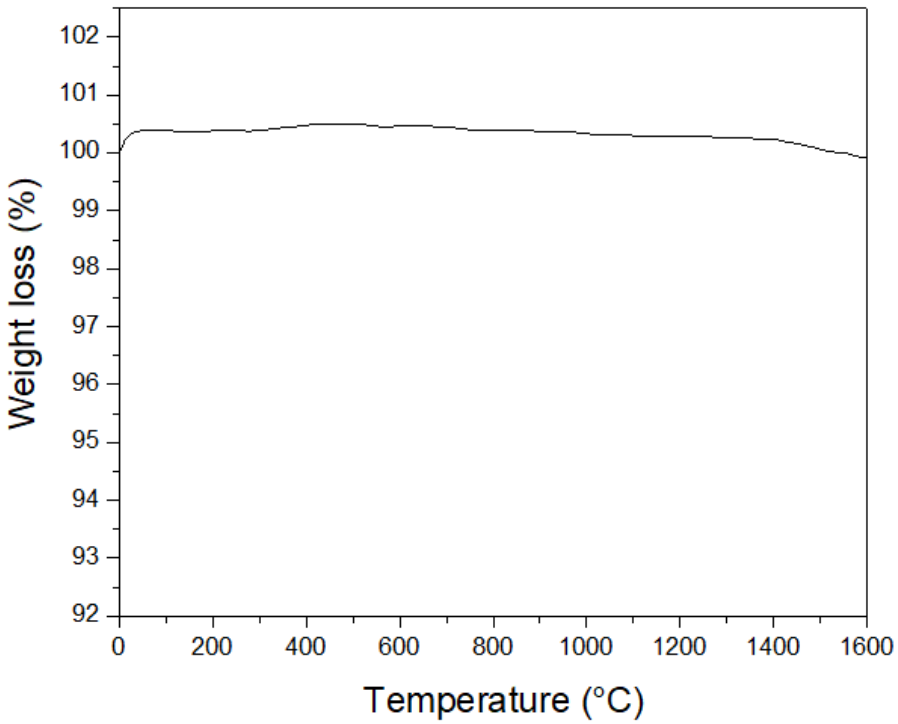

It is possible to see from the graph that there is no significant change in the material`s mass with the increasing temperature up to 1600 C, varying less than 0.5%. This infers that during the sintering process, the material doesn`t dust off or burns, as expected.

Figure 35 shows the differential thermal analysis (DTA) of MS powder, obtained at temperature of 25–1600 °C, on heating, and 1600–200 °C, on cooling, with a heating rate of 5 °C /min. There is no evidence of water evaporation (slight endothermic peak until ~200 °C), which is in accordance with TGA curve (Figure 35). However, above 800 °C up to about 1200 °C, a broad exothermic peak is observed, as a result of surface crystallization of β–cristobalite, followed by fusion at ~1500 °C, which were shifted to lower temperatures. On the other hand, upon cooling, β–cristobalite phase remains metastable up to ~400 °C, when experiences an earlier inversion to low temperature α–cristobalite phase, since according to the literature, the β–α transition generally occur at 170–270 °C, and is accompanied by a reduction in volume. [60].

Figure 35 - DTA of microsilica (MS) powder with a synthetic air flow rate of 100 mL/min and a heat rate of 5 °C/min from 0 up to 1600 °C.

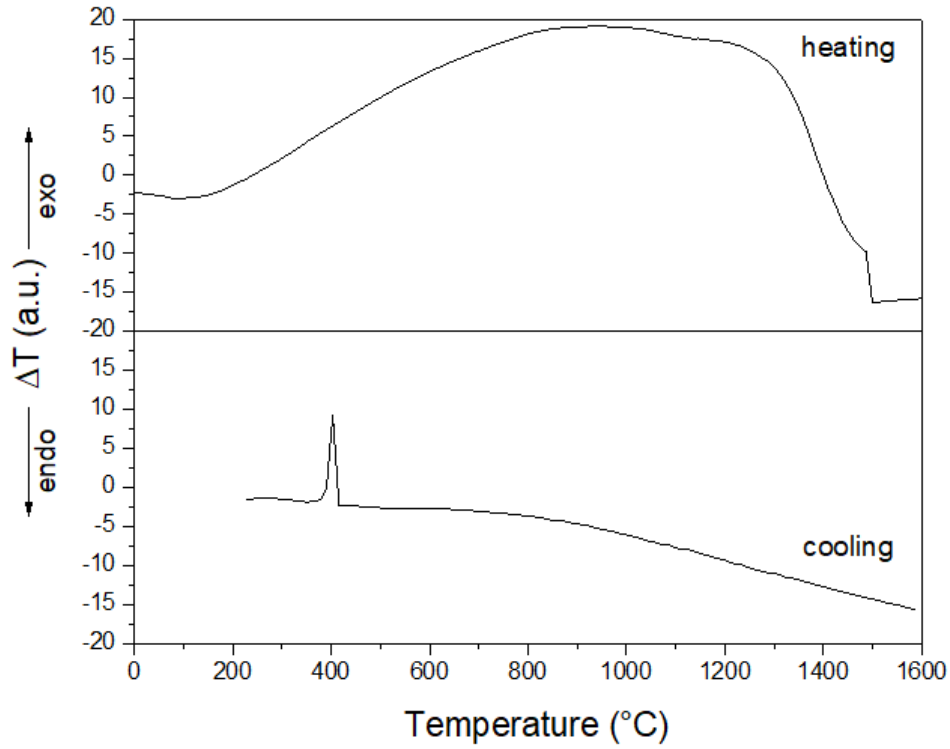

As the size scale changes, the properties of materials alter. For this reason, when working with nanomaterials, features such as melting point, fluorescence, magnetic and electrical conductivity and chemical reactivities present some unexpected behavior. [61] One key property is the so-called melting-point depression, meaning that they melt at lower temperatures than bulk amounts of the same material. Changes in melting point occur because nanoscale materials have a much larger surface-to-volume ratio than bulk materials, drastically altering their thermodynamic and thermal properties. [62]

The thermogravimetric analysis (TGA), Figure 36, reveals that silica nanoparticles (NS) are very stable, and exhibit similar behavior of MS powder, i.e., there is no significant change in the weight of NS with the increasing of the temperature up to 1600 °C.

Figure 36 - TGA of nanosilica (NS) powder with a synthetic air flow rate of 100 mL/min and a heat rate of 5 °C/min from 0 up to 1600 °C.

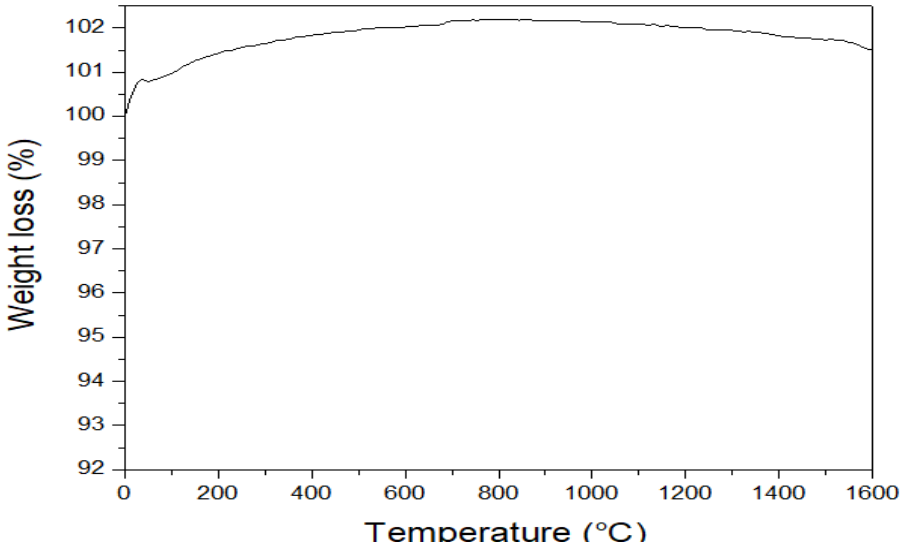

The DTA data of NS is shown in Figure 37. As previously discussed, the thermal behavior of NS and MS on heating from 25 to 1600 °C, is rather similar to each other, except that a narrower exothermic peak in the range of 1100 to ~1200 °C is observed, as a result of surface crystallization of β–cristobalite, followed by fusion at ~1550 °C. These transitions generally occur at higher temperatures (>1470 °C), but were shifted to lower temperatures, probably due to the presence of Si-OH groups and lower amount of oxygen vacancies. [63]. Interesting to note the absence of the exothermic peak related to β–α transition, on cooling at ~170–270 °C. [60]

Figure 37 - DTA of nanosilica (NS) powder with a synthetic air flow rate of 100 mL/min and a heat rate of 5 °C/min from 0 up to 1600 °C.

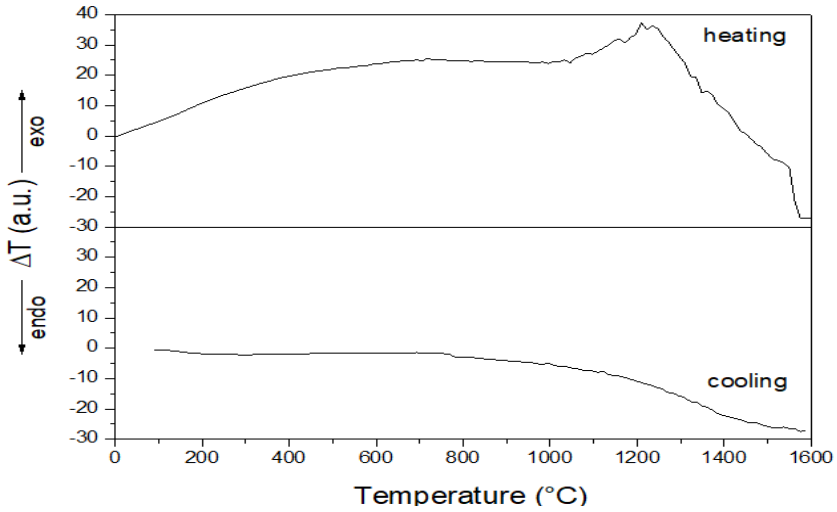

The TGA curve (Figure 38) for NMS powder exhibit two steps of thermal degradation, the first one occurring at lower rate up to ~200 °C, is qualitatively obtained as a result of the loss of physisorbed water and probably ethanol, which comes from the NMS preparation method [64].

The second step starts above 200 °C up to ~600°C, when a fast weight loss occurs (at high rates), which can be attributed to evaporation of chemically adsorbed water molecules, surface dehydroxylation of silica, as well as decomposition of small proportions of organic content from surfactant [65]. After elimination of water and additives, no weight loss was observed, being restricted to the first events and at a value of ~7 %.

The TGA results are consistent and corroborated by the DTA (Figure 39), on heating, which exhibits a characteristic endothermic peak when the temperature reaches 200 °C, related with evaporation of physisorbed water and ethanol. In addition, it is possible to observe two exothermic events, a first one between 200–400°C, related with loss of chemically adsorbed water and surface dehydroxylation of silica. The second exothermic event starts at ~1000 °C up to 1300°C without weight loss associated, as a result of surface crystallization of β–cristobalite, followed by fusion at ~1500 °C. As already pointed out, this crystallization usually occurs at higher temperatures (>1470 °C), but due to the small particle size (in the nanometric range), silica can crystallize at lower temperatures [63]. Interesting to note the presence of the exothermic peak related to β to α–cristobalite transition phase, on cooling at ~200 °C. [60].

On the basis of the discussed above, it can be highlighted that the presence of cristobalite phase was also consistent with XRD patterns.

Figure 38 – TGA of nanosilica-coated microsilica (NMS) powder with a synthetic air flow rate of 100 mL/min and a heat rate of 5 °C/min from 0 up to 1600 °C.

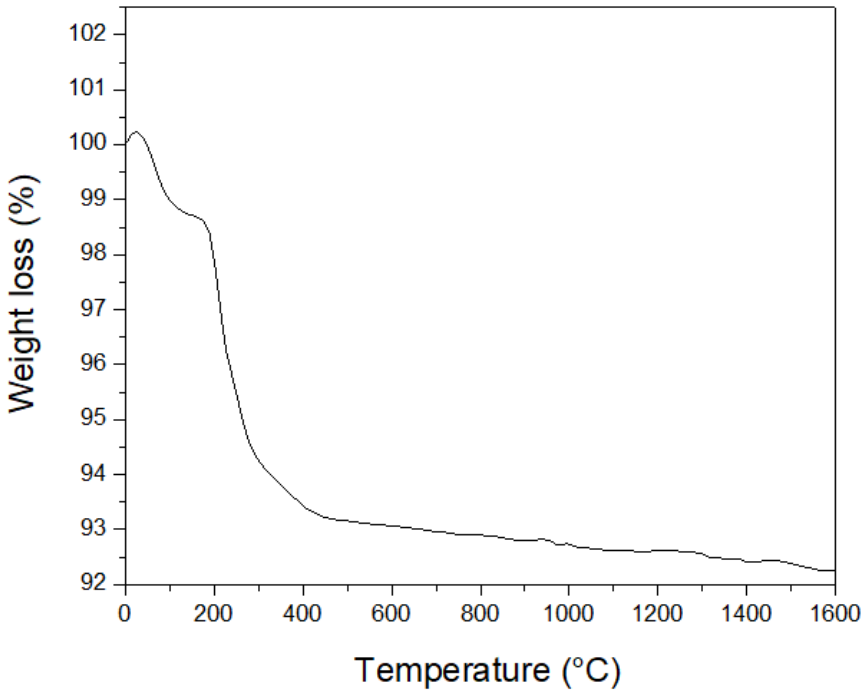

Figure 39 – DTA of nanosilica-coated microsilica (NMS) powder with a synthetic air flow rate of 100 mL/min and a heat rate of 5 °C/min from 0 up to 1600 °C.

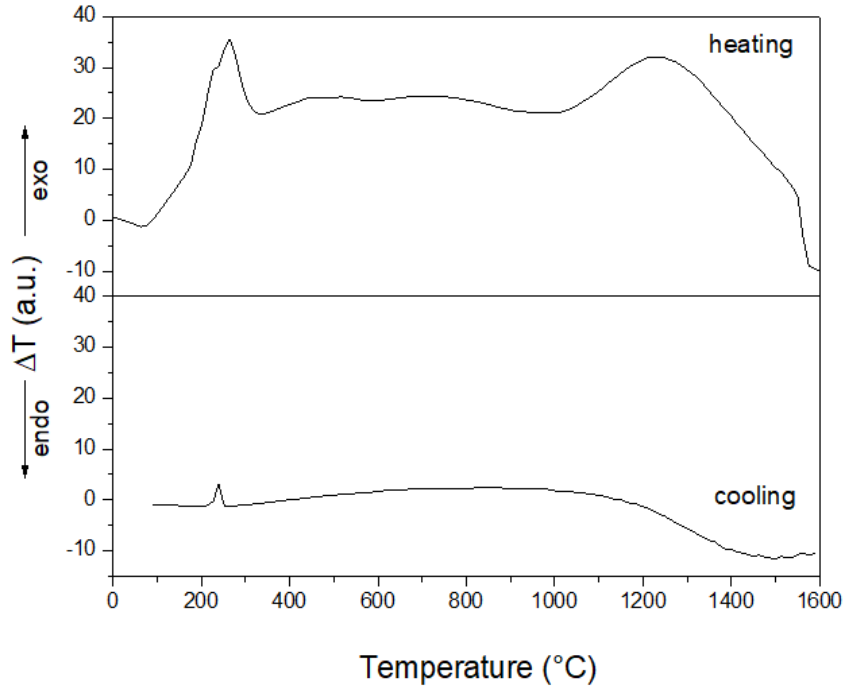

After thermal analysis, X-ray diffraction (Figure 40) shows patterns of the NMS (as prepared) and of the thermally treated SiO_2 samples. For both samples, diffractograms exhibit a diffuse amorphous background. After vacuum sintering at 120 °C (2 h), 350 °C (2 h), 1250 °C (4 h) and 1500 °C for 1h, it is possible to observe the slight peaks formation, mainly at θ= 21.87° at (101) the primary diffraction peak, which are attributed to cristobalite phase (JCPDS 00-039-1425). [66] It is interesting to highlight that the devitrification of amorphous silica is sensitive to moisture in the air and trace impurities [67] such as flux additives (Na+, K+, Li+, etc.), which can favor the transition to crystalline species by collapsing the Si-O-Si bridges of glass network [68] [51]. In addition, according to Breneman and Holloran (2014), seeding of fully amorphous silica powders with cristobalite powder lowers the transformation temperature to 1370 °C (in a conventional box furnace), since it is widely known that cristobalite preferentially nucleates at the surface. [67]

Figure 40 - XRD patterns for as prepared NMS and sintered SiO_2 samples. (Cristobalite; JCPDS # 039-1425).

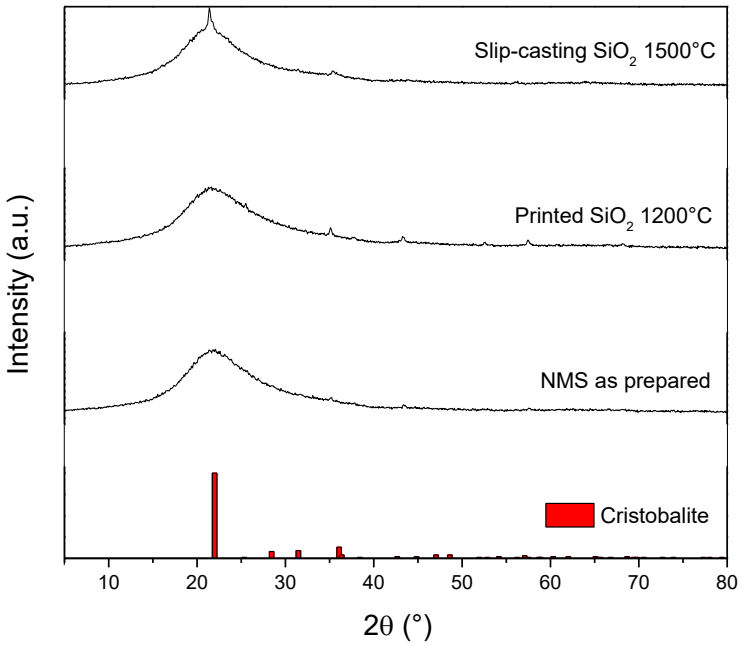

The relative percentage of the amorphous phase regarding to the crystalline phase (cristobalite) was estimated based on the ratio of the amorphous background area over the total area, i.e., the sum of the crystalline and amorphous areas of XRD patterns. [51] The obtained values of amorphous and crystalline phases are given in Table 10. It is interesting to highlight that the nanosilica-coating processing (high energy planetary milling) do not affect the amorphous structure of the silica powders. In addition, there is no evidence of high aluminum contamination on diffractograms, as observed by EDS analysis (see later).

Table 10 - Degree of Crystallinity in NMS powder; slip-cast and 3D printed parts, both fired at 1000 °C.

Sample	**Degree of crystallinity (%)**
NMS powder	0.90
Printed SiO_2 and fired at 1500 °C	4.94
Slip-cast SiO_2 and fired at 1200 °C	6.91

4.2. Characterization of Slip-Cast samples

4.2.1. Density of samples

For the analysis of the slip casting process, two disks produced from the same batch were chosen, and no significant differences should be noticed between each one. No more were evaluated due to the necessity of similar dimensions, even though more successful samples were obtained. Porosity information was gathered for the sintered slip-cast parts through Archimedes method and for the NMS powder gas picnometry was used. As the powders used had the density information on their data sheets, the density measurement should not have a divergent result. For the nanopowder NS, the value is approximately 2.2 g/cm^3 and for the micropowder, 1.25 g/cm^3. The measurement information is presented in Table 11 as well as the density calculated according to Archimedes method.

Table 11 – Apparent density calculation for sintered (at 1500 ºC) slip cast disks.

Parameter	**Disk A**	**Disk B**	**Water Density (g/cm^3)** **At 25°C**
m_{dry} (g)	3.931	3.862	0.997044
$m_{immerse}$ (g)	2.155	2.113	
Density (g/cm^3)	2.206	2.201	

As it can be seen, the results for both disks are very similar and can even be considered the same. It is a good indicator that the parts were fully densified during the sintering process, as they have almost the same dimensions. Comparing to the manufacturer's data, the results are coherent.

4.2.2. Optical Properties of Sintered samples

Two transparent sintered, slip cast parts were used for the optical properties' determination. Both disks were obtained from the same processing and firing process. There should be no significant difference between them, so the idea is to use more than one to compare reproducibility of the process as a whole. Each disk was analyzed in three different regions, in order to have an overall idea of the whole body and the mean value calculated. They can be seen in Figure 41.

Figure 41 – Photography showing transparent silica sintered slip-cast samples fired at 120 °C (120min), 350 °C (60min), 1250°C (240min) and 1500 °C (60min). Disk 1 (left) with a 23.10 mm diameter and 4.50 mm thickness and Disk 2 (right) with a 23.01 mm diameter and 4.52 mm thickness.

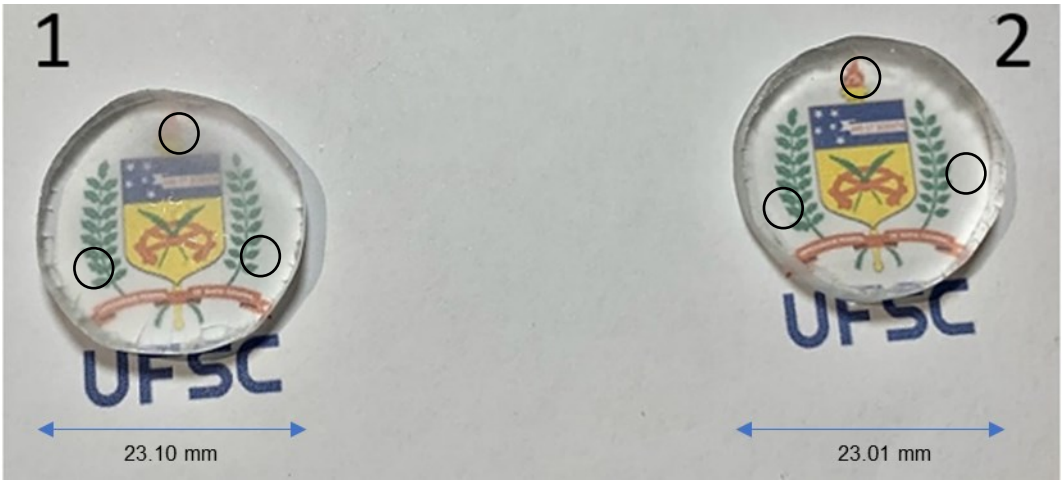

A few visible aspects can be discussed over the images. It is possible to see that there is a present of a blur, or a mist inside the parts. Also, the edges present small cracks with white lines and a few hypotheses are raised. The mist is possibly the beginning of the formation of small crystals, due to incomplete densification and the presence of pores inside the parts. Several literatures point out the possibility of the formation of crystallization before complete sintering and point out that exists a “race” between each mechanism [69] [70] [71]. The cracks probably occur because of the same reason, which is a trigger for crystallization and consequently the formation of white like polymorphs, removing the transparency. Although there are some defects on the slip-cast parts, the results present a visually satisfactory aspect, as the UFSC logo and what is beneath can be easily seen and read, with no large distortions.

For opacity measurement, the data is given directly by the equipment and is expressed in Table 12, together with the dimensions of the disk samples.

Table 12 - Opacity of silica sintered slip-cast disks.

	D65/10º	**A/10º**	**CWF/10º**
DISK 1			
Diameter (mm)	23.10		
Thickness (mm)	4.50		
Opacity (%)	21.125	20.975	21.050

DISK 2			
Diameter (mm)	23.01		
Thickness (mm)	4.52		
Opacity (%)	22.518	22.359	22.438

Opacity is related to the coverage of what's behind the material being studied, and the thickness of the material influences the results. The less opaque, the more it can be seen through. To be able to compare different parts, they must have similar dimensions, otherwise the results may not be reliable. For disk 1, the values for all light sources are practically the same, at around 21% and can be interpreted that for different environments, the transparent parts are not affected significantly. The same can be said for disk 2, although the value increases slightly approximately 22%. Those values are corroborated by Figure 42 (black-white or slip), where the background can be seen through rather significantly.

Figure 42 – Photography showing transparent silica slip-cast disks 1 (left) with a 23.10 mm diameter; disk 2 (right) with 23.01 mm diameter over a background is the paper for black and white quantification for TP index, and it is from Leneta – Form 2A-H Opacity

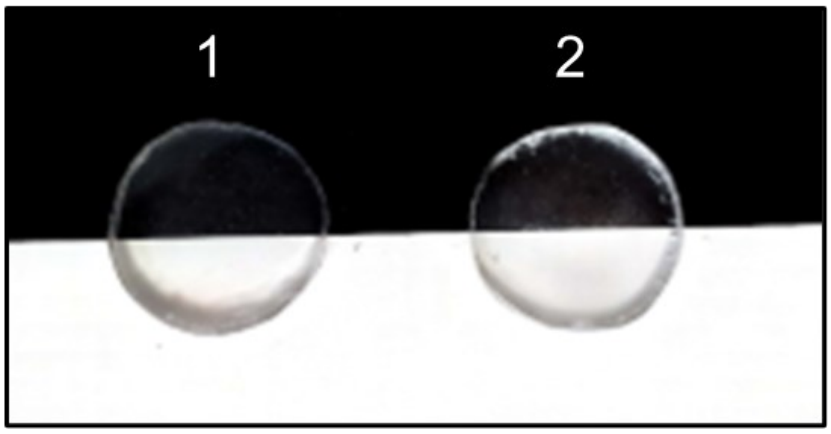

Another optical evaluation is given by the Translucency Index (TP). This index is obtained from an indirect measurement of the Reflectance, which is then calculated using equation 13 to obtain the value. It uses a white and black standard background to measure the values of L*a*b. The usage of a known value background is to be able to obtain the true value of the desired part, by excluding the white and black. The values for the L*a*b as well as for the TP index are expressed in Table 13, for two disk samples, respectively:

Table 13 - Translucency Index (TP). of silica sintered slip-cast disks.

		L	A	B	C	TP
DISK 1						
D65/10°	w	78.76	-1.31	2.45	2.78	38.51
	b	40.43	-0.315	-1.10	1.15	
A/10°	w	78.79	-0.392	2.06	2.09	38.62
	b	40.31	-0.616	-1.24	1.38	
CWF/10°	w	78.75	-0.932	2.62	2.78	38.60
	b	40.36	-0.206	-1.26	1.28	
DISK 2						
D65/10°	w	73.87	-1.223	2.28	2.60	35.60
	b	38.46	-0.248	-1.16	1.18	
A/10°	w	73.90	-0.357	1.91	1.94	35.69
	b	38.34	-0.560	-1.28	1.40	
CWF/10°	w	73.86	-0.869	2.43	2.59	35.68
	b	38.39	-0.159	-1.32	1.33	

The measurements were obtained for three different light sources (D65/10º, A/10º and CWF/10º), from 3 different areas on each disk and the mean values displayed on correspondent tables. For disk 1, it is possible to observe that there was no significant variation in the TP index, staying at around 38.60. As for disk 2, the evaluation remains the same, only the values change a little, but not significantly. The results for all light sources are at around 35.65, only 7.5% less than the results for disk 1.

The results can be compared to the study provided by Ledic et al. (2015). The evaluation provided by the authors showed that glass-ceramics (IPS) for dental applications presented values of TP ranging from 7.58 up to 16.50. The data obtained with the silica materials had significantly higher values and, as mentioned before, can be considered more translucent.

4.3. Characterization of 3D-Printed Bodies

4.3.1. Dilatometry

Figure 43 shows the linear shrinkage curves of sodium alginate and PVA gel suspension filaments compacts. According to the dilatometric curve of sodium alginate compacts (red curve), there are no significant changes in the dimensions up to about 250–300 ºC. However, above this temperature range up to about 450 ºC, a slightly expansion (less than 1%) occurs, this may be attributed to surface dehydroxylation of silica, and to the decomposition of alginate characterized by carbonaceous gas evolution and sodium oxide residue formation. [72] [73]. In addition, sodium alginate compacts start to densify at 500–700 ºC that is characterized by shrinkage of about ~2%. On the other hand, dilatometric curve of PVA gel suspension compacts, blue curve on Figure 41, exhibit a first expansion at 100–300 ºC, which can be related to the evaporation of water and elimination of acetate groups. Furthermore, a second expansion occurs (~1.5%) from 400–900 ºC, which may be related to the overlap of a continual degradation of residual acetate groups and chain-scission reactions [74]. From this temperature range up to about 1200 ºC, a shrinkage of about ~5% occurs, which can be associated to fast densification.

Thus, from the results presented by both gel suspension filaments, it is interesting to highlight that the higher concentrated PVA gel filaments present higher amount of volatile substances under thermal degradation, when comparing with alginate gel filaments. On the other hand, the presence of fluxing additives, especially Na_2O, on alginate gel suspension, induced first densification step at lower temperatures. [51]

In summary, densification did not occur at temperatures lower than 1200 ºC supporting the fact that silica has the ability to keep chemically adsorbed water for long time and at high temperatures exhibiting a good thermal stability. [75]

From the discussions of the results presented by NS, which continues at lower rates up to ~830 ◦CA slight increase in volume is observed from above 900 ◦C, as a result of the viscous liquid phase formation from the melting of the crystalline phases present. associated with dehydration and evaporation of water molecules as well as the.

Figure 43 – Dilatometry comparison: NMS filaments based on Sodium alginate and PVA gels.

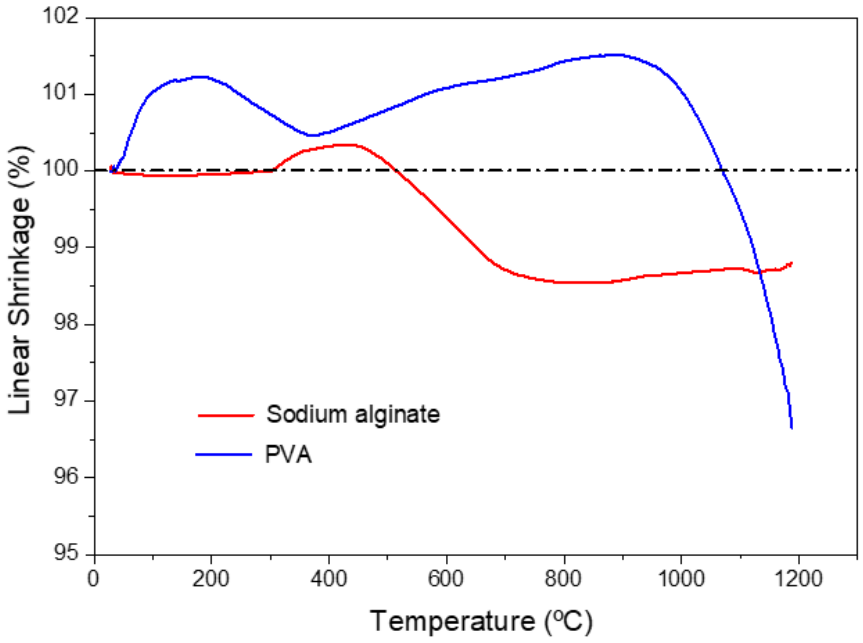

Sudden changes (expansion/shrinkage) in the structure could cause cracks and the formation of extreme porosity inside the filament, which could consequently decrease mechanical properties.

4.3.2. Density and Porosity of Sintered Bodies

The density and porosity of the sintered, 3D-printed parts based on PVA and sodium alginate dimensions are presented in Table 14:

Table 14 – Porosity of sintered, 3D-printed sodium alginate part (50% wt solids – 50% wt liquid) fired at 650 °C (120 min) and 1200 °C (120 min).

Parameter (Unit)	**Value**
Length (mm)	23.76
Width (mm)	23.00
Height (mm)	6.95
Volume (cm^3)	3.80
Mass (g)	2.87
Geometric Density (g/cm^3)	0.755
Picnometric Density (g/cm^3)	2.41
Porosity (%)	68.66

As previously mentioned, the nano and micro powders present a density ranging from 1.25 up to 2.2 g/cm^3. As for the robocasting technique NMS powder was prepared, the density had to be measured, and the value of 2.41 g/cm^3 is coherent with the original raw materials. As for the porosity, a value of approximately 69 % is observed, taking into account that for the printed parts additives were used and removed during the thermal procedure, leaving the pores open. This as a result is significant, mainly due to the fact that the idea to produce 3D printed silicon dioxide parts were to use them as drug carriers or as scaffolds for bio applications, where porosity is desired.

The picnometric density of 2.41 g/cm^3 is the same for PVA robocast parts, as well as the variables used. The results for such part are displayed in Table 15.

Table 15 - Porosity of sintered, 3D-printed PVA part (65% solids – 35% liquid) fired at 650 °C (120 min) and 1200 °C (120 min).

Parameter (Unit)	**Value**
a (mm)	27.05
b (mm)	27.19
h (mm)	8.98
Volume (cm^3)	6.60
Mass (g)	3.89
Geometric Density (g/cm^3)	0.589
Picnometric Density (g/cm^3)	2.41
Porosity (%)	75.56

The PVA part was printed with bigger dimensions, due to operational variables. The final porosity was higher compared to sodium alginate with a value of around 76%. Comparing the two structures, it is possible to assume that PVA originated parts is less dense and consequently has more pores. This difference can be attributed to different factors demonstrated through the analysis: firstly, the viscous suspension used affects the drying step differently, and the water evaporation leave bigger gaps. Also, the solids loading of PVA parts is higher, but a big part of it is originated from the PVA, with 20% solids content, where for sodium alginate it is limited at 6%. Secondly, the amount of additives (methyl cellulose) used for each process is different and it is another material to leave the structure in the thermal step of the process. Summing all these

aspects, it is expected to have a higher porosity in PVA originated parts than sodium alginate ones and the benefits or setbacks linked to porosity for the desired applications can be further studied.

4.3.3. Structures of Green and Sintered Parts

As for the 3D printed bodies, the evaluation of the results was conducted after each step of the procedure: right after printing, after drying and after firing. Figure 44 shows the whole process: from just printed (a), to drying procedures (b) for room temperature and 24 h drying and (c) 3 h drying at – 42 °C and lyophilization for 24h at – 42 °C and 100 mbar vacuum (LJJ from JJ Cientifica), until the final post firing and final product (d) fired at 650 °C (120 min) and 1200 °C (120 min).

Figure 44 – Photograph showing 3D-printed sodium alginate samples. (a) right after shaping, (b) room temperature drying (c) freeze dried and (d) post firing final body.

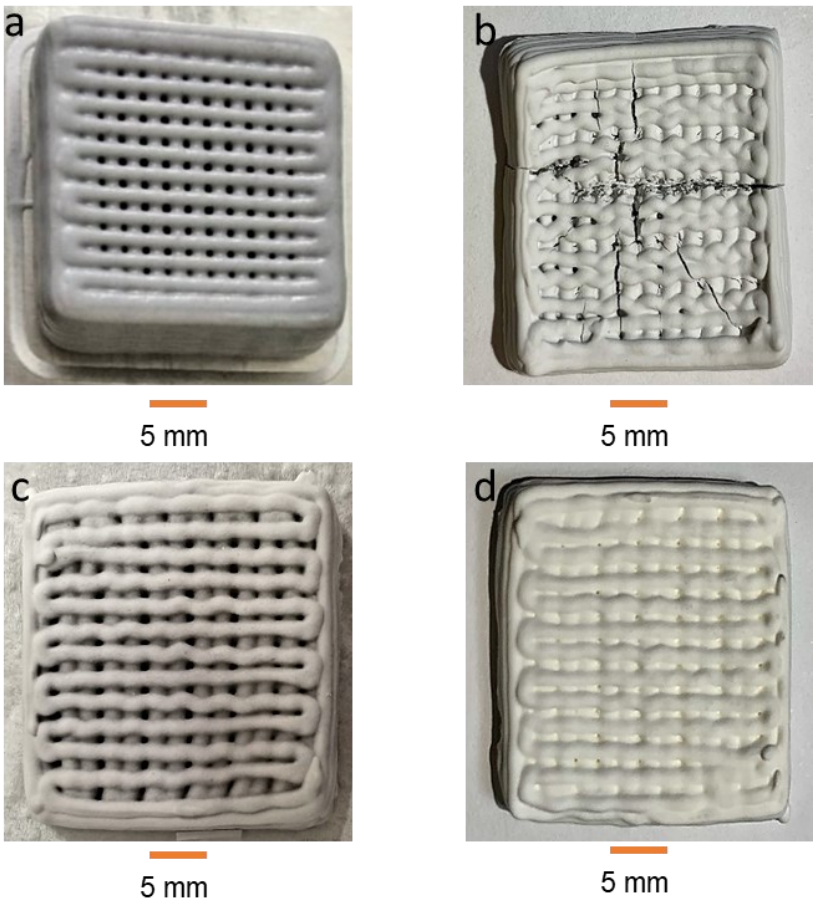

As from observed in 44.a, it was possible to build some macropores, but due to the rather liquid aspect of the suspension, most of them closed right after the layer deposition. The next crucial step is the drying of the printed part. As it involves the removal of water from the part, if not properly conducted, can cause cracks and compromise the whole structure. For this procedure,

two different techniques were used, in order to explore options. Firstly, the parts were put inside a humidity control chamber and left to dry at room conditions.

It is possible to observe from 44.b that for sodium alginate parts the room conditions do not provide a controlled environment for the parts to dry without cracks. As an alternative, a freeze-drying process, as explained previously, was chosen, to freeze the inside liquid and be removed under vacuum. The structures were put inside the freezing chamber for a period of 3 h at a – 42 ºC temperature. Afterwards, they were put in the vacuum environment of and 100 mbar vacuum and went through lyophilization for 24 h, as shown in Figure 44.c

The results for this method are significantly better. It does not seem to present any visible cracks and the structure was maintained. As a bonus, this technique is used to produce unidirectional pores, which can be beneficial for applications such as drug delivery systems or scaffolds.

After the drying procedures, the bodies were fired at 650 °C (120 min) for water and additives elimination and 1200 °C (120 min) for sintering. The result can be seen in Figure 44.d. The final sintered parts didn't present either visual shrinkage or cracks. The white color indicates the formation of crystal polymorphs of silica, which are further investigated in the characterization part of this work.

The second experiments were performed using PVA gel as the liquid part for the suspension. The preparation was similar, with different concentrations. As the PVA gel presents a more liquid aspect, the solids:liquid ratio was increased to 65:35, being the NMS powder and the PVA solids portion counted towards the first and the water towards the second segment of the ratio. A total of 2 % of solids of methyl cellulose was added to increase viscosity. The final suspension was stickier than the sodium alginate one.

For the robocasting process it was chosen the same 1.11 mm nozzle, changing the initial pressure up to 2 bar and maintaining the printing speed at 10 mm/s. This increase in pressure can be attributed to the glue-like aspect of the suspension, which requires a bigger initial push for the material to start flowing and depositing. The whole process can be observed in Figure 45, where (a) corresponds to the parts right after shaping, (b) to room temperature drying for 24 h, (c) to parts frozen at – 42 °C for 3 h and lyophilized at – 42 °C and 100 mbar vacuum for 24h and (d) 3D-printed PVA-gel based body fired at 650 °C (120 min) and 1200 °C (120min)

Figure 45 – Photography showing 3D-printed sodium alginate samples. (a) right after shaping, (b) room temperature drying (c) freeze dried and (d) post firing final body.

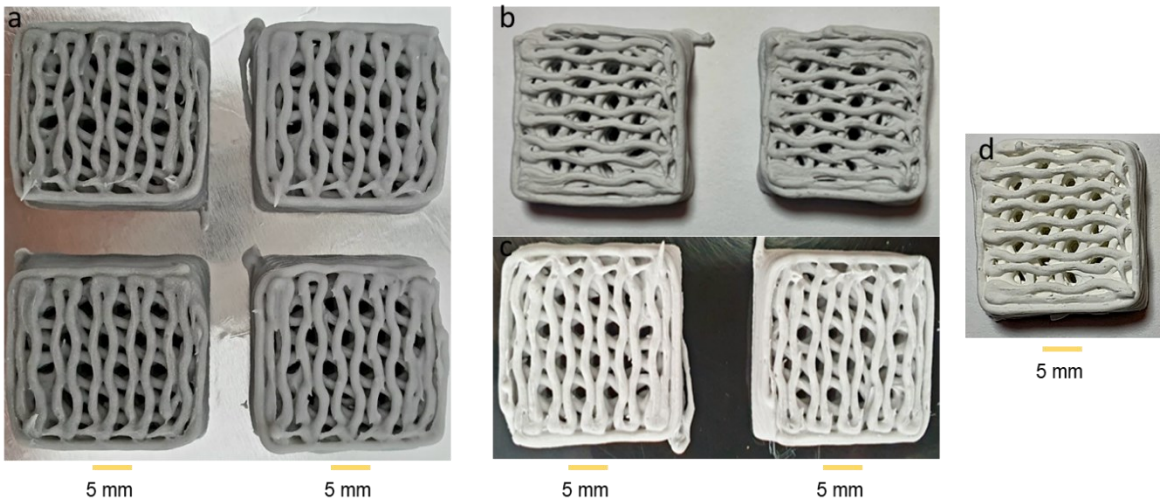

Using PVA gel as suspension has allowed the robocasting process to go a little more automatically, as there is a higher predictability and no need in parameter change of printing variables mid process. As a result, the printer could produce 4 parts at a time. As it can be seen in 45.a, the parts are similar but not the same and this can be related to the fact that the suspension is still in development. Even though, when comparing to the recently printed sodium alginate part, these could maintain a wider macro porous structure just after the printing process. These four parts were separated in pairs and put to different drying conditions, being two sent to the humidity control chamber at room temperature (45.b) and the other towards the freeze-drying process (45.c).

It is possible to observe that differently from sodium alginate parts, the results seem the same when comparing drying processes. Both drying procedures are apparently successful and preserve the original macro porosity as well as the overall structure of the parts. For the drying, without taking into consideration further applications, that both methods are sufficient for the PVA gel robocast parts. Afterwards, the parts went to the thermal process of firing.

There is only the representation of one of the sintered parts (45.d), as the other one was sliced to analyze in the SEM microscope. The visual results are similar for PVA as it was for sodium alginate. There was no apparent shrinkage and visible cracks. The white color indicates that the amorphous polymorph went through a phase change, possibly due to the micro and macro porosity created by the additives and designed printed structure. Further investigation with a more thorough background is given in the following topics.

4.3.4. Microstructures of Sintered Parts

As it was previously mentioned, the freeze-drying technique was chosen to improve the drying process of 3D printed parts, to minimize the formation of cracks. Another feature of such technique is the possibility in forming unidirectional pores, beneficial for medical applications, such as drug delivery or scaffold for bioimplants. It was possible to observe visually that the cracking for sodium alginate parts were mostly eliminated and no significant change for PVA gel parts, but for unidirectional micro-porosity and morphological structure, SEM analysis was conducted. For the chemical composition, EDS was applied. The 3D sodium alginate sintered parts are shown in Figure 46, followed by the EDS analysis in Figure 47.

Figure 46 – SEM images of sintered sodium alginate 3D-printed sample with a) 100x, b) 500x and c) 1000x magnifications.

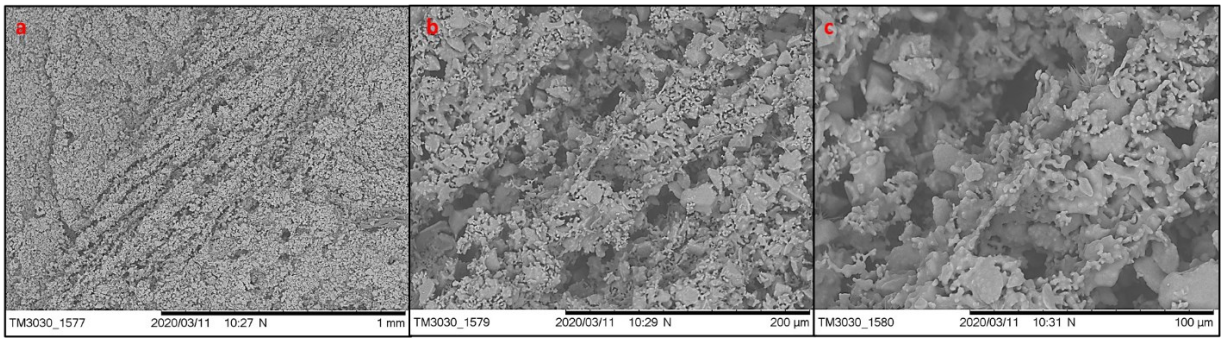

Figure 47 – Chemical composition (EDS) of sintered 3D-printed sodium alginate sample with 1000x magnification

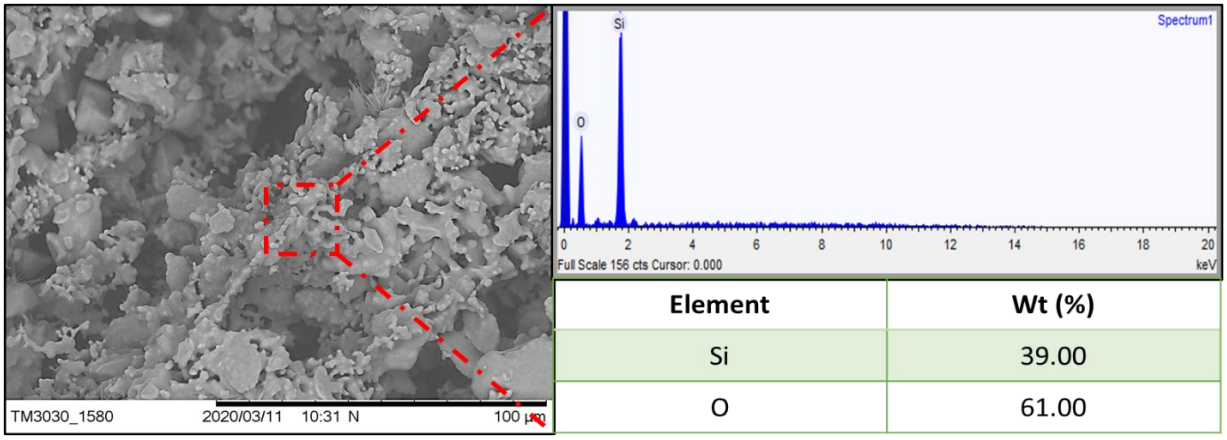

Element	Wt (%)
Si	39.00
O	61.00

As it can be seen from the SEM imaging, there is no visible unidirectional organization of pores, although it was a viable and effective option to drying the parts. The zoom of 1 mm, 200 µm and 100 µm, from left to right also provides information on how the NMS works with the attachment of NS into NMS, which is confirmed and further approached by FESEM images. As for EDS, a small portion of carbon present was disregarded, as it was considered to be the carbon tape background. The percentages of 39% silicon and 61% oxygen is coherent with the expected.

PVA gel 3D printed parts were also analyzed, and the images as well as EDS are shown in Figure 48 and 49, respectively.

Figure 48 – SEM images of sintered 3D-printed PVA gel sample with a) 30×, b) 100× and c) 1000× magnifications.

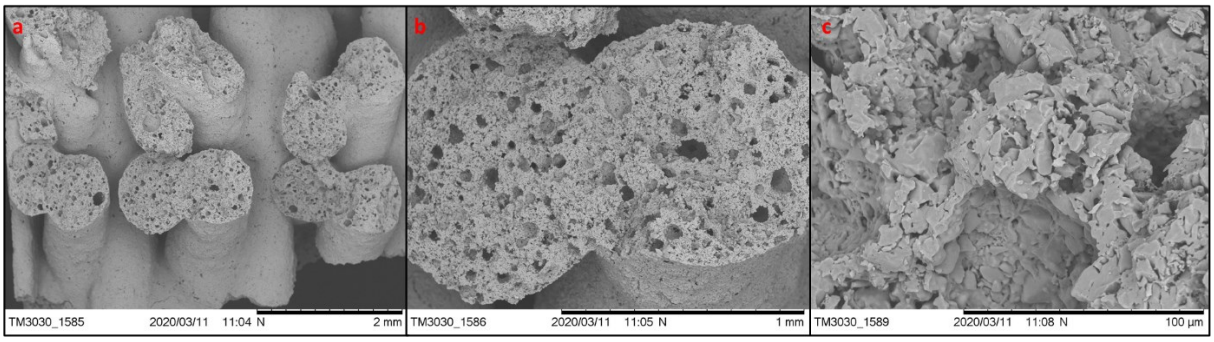

Figure 49 – Chemical composition (EDS) of sintered 3D-printed PVA gel sample with 1000× magnification.

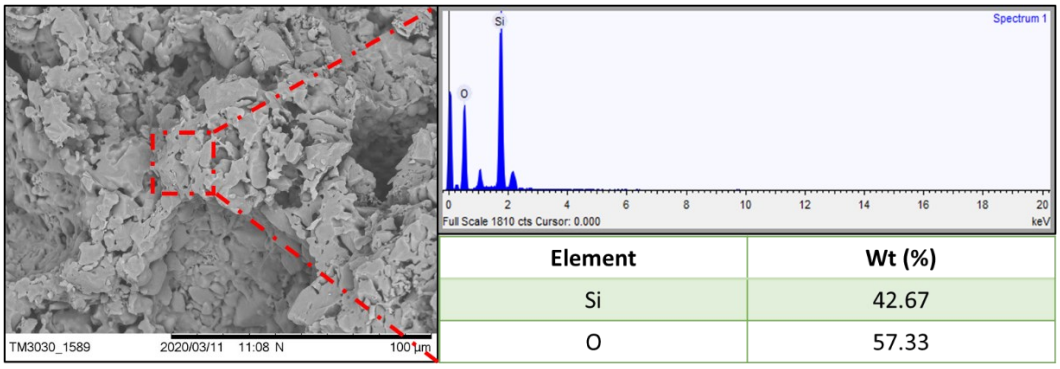

Element	Wt (%)
Si	42.67
O	57.33

For PVA gel 3D printed parts it was necessary to use smaller zooms to observe the structure, going through 2 mm, 1 mm and 100 µm, from left to right, in Figure 48. Unlike sodium alginate parts, it is possible to observe the filament formations, as during the drying they actually maintained the printed form. As the zoom enhances, it is possible to see the formation of inner porosity inside the filament, which could be one of the factors to induce crystallization. As for the EDS analysis, the results are very similar to sodium alginate parts, as it was expected, since the final composition after the thermal process should result only in silicon dioxide.

5. CONCLUSIONS

Ceramic materials have been gaining more and more attention as the technology develops. The broad range of applications from optical fibers up to medical diagnosis justifies the pursuit of novel materials and production methodologies. Silicon dioxide as one of the most abundant material's on Earth's crust has proven to be successful to the production of both transparent densified glass as well as for the printing of scaffolds.

A nanopowder (NS) and a micropowder (MS), as well as a blend of both (NMS) were used for the research. Size distribution and morphological analysis were conducted in order to describe the steady state of each material. SLS and DLS techniques showed that the size distributions were monomodal for the acquired powders and the NMS had a trimodal distribution. TEM images showed a tendency of agglomeration for the powders, that impacted in the overall size distribution and FESEM showed a successful production of the occlusion distribution of NS on the MS surface. XRD analysis showed the transformation from amorphous silica to crystalline, in the final form of cristobalite, that affects the overall transparency of slip cast disks.

Stability was evaluated through Zeta Potential using water suspensions for the three powders and results showed that they were all stable on their working pH, with a value below – 30 mV. Further investigation on stability was given using rheology analysis for the slip casting slurries and the 3D printing suspensions. For the slip casting technique slurries were prepared altering the percentage of solids, while maintaining the overall solid: liquid ratio to 70:30 wt %. The first one consisted of 9% NS and 61% of MS, while the second one of 12 % NS, 61% MS. Results showed a slight increase in viscosity with the greater amount of NS, due to the fact that there is a higher surface area and thus higher collision rate that justifies the increment. Rheology was also studied for the NMS alginate-based suspension as well as the PVA-based. The overall results were similar, with a higher value of viscosity and applied shear rate for the PVA suspension. This may require higher pressures to force the deposition of the suspension, but the suspension is expected to have lower deformation after the printing.

Thermal analyses were conducted in order to study the behavior of silica and the used additives for both slip casting and 3D printing processes. TG and DTA data confirmed the stability of pure MS and NS powders, without any considerable mass loss and the expected phase transition of amorphous to β-cristobalite and later to α-cristobalite at the cooling stage. As for the NMS powder, the results were somewhat richer. It showed the elimination of absorbed water, as well as dihydroxylation and organic residues from surfactant at different temperatures, which were possible to see through mass loss in TGA and corroborated by the presence of an initial endothermic (200 ºC) followed by two exothermic (200 - 400 ºC and 1100 – 1300 ºC) peaks in the DTA data. The phase transition was no different than to the powders being evaluated separately, with crystallization to β-cristobalite and the transformation at lower temperatures to α-cristobalite.

As for the suspension filaments of sodium alginate and PVA, dilatometry showed some changes in each base material due to the presence of more or less volatile materials, there was no significant shrinkage throughout the heating process.

Slip cast transparent disks were studied for its optical properties, evaluating the percentage of opacity and the Translucency Index (TP). Also, the density of the bodies was evaluated, since they affect directly in the resulting transparency. Two disks from the same batch were evaluated to have an idea of reproducibility of the process. The opacity results for both disks showed a value of around 20% and the TP ranged from 35 up to 38. The density results from Archimedes method showed that the final transparent bodies maintained the original powder density of 2.2 g/cm^3.

For the 3D printing technique, two different suspensions were produced: NMS powder with sodium alginate gel and NMS powder with PVA gel. The process consisted of printing, drying and firing, with two different methods to dry: first, room temperature for 24h and secondly freeze drying for 24h at – 42°C and 100 mbar vacuum. Not only the idea of testing different ways of drying, the usage of lyophilization can also be an option to produce unidirectional porosity, beneficial to bio applications. The results for sodium alginate-based parts were significantly different from each drying method, as in room temperature drying cracks were observed in every printed part, while the freeze drying was able to maintain the form. As for the PVA, there were no visible difference in the results. Density and porosity analysis were also conducted in order to have an idea on how much of the specimen consisted of solvent and additives. The densities were similar to the manufacturer data sheet information, and the porosity was of 65% for sodium alginate parts and 75% for PVA. To conclude the analysis, SEM images were used to investigate if the porosity channels were in fact present. For the alginate parts, there was no clear particle organization, while in PVA parts it was clear to see. One of the possible reasons is the rheology of the gels, since the more viscous behavior of PVA was able to have a better maintenance in post 3D printing form.

To conclude, the overall objective of using silica as a raw material to produce ceramic bodies was fulfilled. As for the more specific, traditional technology of slip casting was successful in the production of transparent bodies and 3D printing has proven to be an ongoing and to be further explored technology to produce scaffolds. Further research in slip casting optimization, as in the suspension preparation, stabilization and the exploration of firing procedure can result in even more transparent bodies. Focus on the development of new suspensions and optimization of printing parameters towards bio applications, as referenced in this work, can be extensively explored in the pursuit of new products.

6. REFERENCES

[1] _____, "**History of Glass**" [Online]. Available: http://www.historyofglass.com/. [Accessed 07 2020].

[2] _____, "**HERAEUS CONAMIC**" Properties of Fused Silica, [Online]. Available: https://www.heraeus.com/en/hca/fused_silica_quartz_knowledge_base_1/properties_1/properties_hca.html. [Accessed 2020].

[3] NGUYEN, T; MEYERS, C; UEE, D.; DUDUKOVIC, A.; DESTINO, F.; ZHU, C.; DUOSS, B.; BAUMANN, F, T.; SURATWALA, T.; SMAY E, J.; and DYLLA-SPEARS, D. "**3D-Printed Transparent Glass**," *Advanced Materials,* vol. 29, pp. 1701181 (1-5), 2007.

[4] ZHU, C.; PASCALL, J, A.; DUDUKOVIC, N.; WORSLEY A, M.; , KUNTZ, D, J.; DUOSS B, E.; and SPADACCINI, M, C. "**Colloidal Materials for 3D Printing**," *Annual Review of Chemical and Biomolecular Engineering,* vol. 10, no. 1, pp. 1-26, 2019.

[5] PENG, E.; ZHANG D.; and DING, J."**J. Ceramic Robocasting: Recent Achievements, Potential, and Future Developments. "** *Advanced Materials,* vol. 1, no. 1, pp. 1-14, 2018.

[6] LEI, Q.; GUO, J.; NOUREDDINE, A; WANG, A.; WUTTKE, S.; BRINKER J, C.; and ZHU, J. "**Sol–Gel-Based Advanced Porous Silica Materials for Biomedical Applications**," *Advnced Functional Matherials,* no. 1, 2020.

[7] AL-HASNAWI K.; and AL-HYDARY, D."**The devitrification kinetics of transparent silica glass prepared by gel-casting method,**" *Revista Matéria,* vol. 24, no. 1, 2019.

[8] REGI-VALLET M.; and BALAS, F. "**Silica Materials for Medical Applications**," *The Open Biomedical Engineering Journal,* vol. 2, no. 1, pp. 1-9, 2008.

[9] PUBCHEM, "**Silicon Dioxide**," [Online]. Available: https://pubchem.ncbi.nlm.nih.gov/compound/Silicon-dioxide. [Accessed 01 2020].

[10] FLORKE, W. "**Silica,"** in *Ullmann's Encyclopedia of Industrial Chemistry*, Weinheim, Wiley-VCH, 2008, p. 455.

[11] BARTHEL, H.; ROSCH L.; and WEIS J. "**Fumed Silica – Production, Properties and Applications**", Wacker-Chemie, 1996.

[12] HENCH, L.; and BEST, M. "**Ceramics, Glasses and Glass-Ceramics**," *Biomaterials Science,* pp. 128-151, 2013.

[13] LEWIS, A."**Colloidal Processing of Ceramics**," *Journal of American Ceramics Society,* vol. 83, no. 10, pp. 2341-2359, 2000.

[14] MORENO, R.; FARIÑAS, C.; MOERMET, M, J. "**Effect of Colloidal Stability of Ceramic Suspensions on Nebulization of Slurries for Inductively Coupled Plasma Atomic Emission Spectrometry**," *Journal of Analytical Atomic Spectrometry,* vol. 9, pp. 841-849, 1994.

[15] FISHER, L.; COLIC, M.; RAO, P.; and LANGE, F. "**Effect of Silica Nanoparticle Size on the Stability of Alumina/Silica Suspensions**," *Journal of American Ceramic Society,* vol. 84, no. 4, pp. 713-718, 2001.

[16] JÚNIOR, A, B, B. "**The Behavior of Zeta Potential of Silica Suspensions**," *New Journal of Glass and Ceramics,* vol. 4, no. 1, pp. 29-37, 2014.

[17] MEZGER, T, G. "**The Rheology Handbook**." 4th Edition, Vicentz Network, 2014.

[18] HEINRICH, G, J.; and GOMES, M., "***Einführung in die Technologie der Keramik,"*** 2014.

[19] JERMAN, E.; "***Additive Fertigung von transparenter Siliziumdioxid-Keramik mittles lageweise augebrachter Schlickerdeposition."***

[20] LEE, J, D.; SO, J, H.; YANG, S, M., "**Rheological behavior and stability of concentrated silica suspensions**," *Journal of Rheology,* vol. 43, no. 5, pp. 1117-1140, 1999.

[21] TANNER, I, R.; and WALTERS, K., "**Some distinctive rheological concepts and phenomena**," in *Rheology: An Historical Perspective*, Elsevier Science, 1998, pp. 159-186.

[22] MANGESANA, N.; CHIKUKU, S, R.; MALNZA, N, A.; GOVENDER, I.; VAN DER WESTHUIZEN, P, A., "**The effect of particle sizes and solids concentration on the rheology of silica sand based suspensions**," *The Journal of The Southern African Institute of Mining and Metallurgy,* vol. 108, no. 4, pp. 237-243, 2008.

[23] SCHILLING, C, H., "**Colloid Casting**," in *Encyclopedia of Materials: Science and Technology*, Pergamon, 2001, pp. 1314-1319.

[24] TOFAIL, A, M, S.; KOUMOULOS, P, E.; BANDYOPADHYAY, A.; BOSE, S.; O`DONOGHUE, L.; and CHARITIDIS, C., "**Additive manufacturing: scientific and technological challenges, market uptake and opportunities**," *Materials Today,* vol. 21, no. 1, pp. 22-37, 2018.

[25] ZOCCA, A.; LIMA, P.; and GÜNSTER, J., "**LSD-based 3D printing of alumina ceramics**," *Journal of Ceramic Science and Technology,* vol. 8, no. 1, pp. 141-147, 2017.

[26] RODRIGUES, P, V.; ZANCUL, S, E.; MANÇANARES, G, C.; GIORDANO, M, C.; and SALERNO, S, M., "**Manufatura aditiva: estado da arte e framework de aplicações**," *Gepros,* vol. 12, no. 3, pp. 1-34, 2017.

[27] CALVERT, P., "**Freeform Fabrication**," in *Encyclopedia of Materials: Science and Technology*, Pergamon, 2001, pp. 3340-3347.

[28] PROTOTYPES, A., "**Stereolithography**," [Online]. Available: https://www.axisproto.com/solutions/sla/. [Accessed 02 2020].

[29] KITSAKIS, K.; MOZA, Z.; IAKOVAKIS, V.; MASTORAKIS, N.; AND KECHAGIAS, J., "**An investigation of dimensional accuracy of Multi-Jet Modeling parts**," *Mathematical Models and Computational Methods,* vol. 1, no. 1, pp. 151-157, 2015.

[30] MASOOD, S, H., "**Advances in Fused Deposition Modeling**," *Comprehensive Materials Processing,* vol. 10, no. 1, pp. 69-91, 2014.

[31] EBERT, I.; OZKOL, E.; TELLE, R.; and FISCHER,H., "**Direct Inkjet Priting: a versatile method of complex shape manufacturing**," *Conference Paper - 10th International Conference of the European Ceramic Society,* vol. 1, no. 1, pp. 637-640, 2008.

[32] KRUTH, P, J.; MERCELIS, P.; VAN VAERENBERGH, J.; FROYEN, L.; and ROMBOUTS, M., "**Binding mechanisms in selective laser sintering and selective laser melting**," *Rapid Prototyping Journal,* vol. 11, no. 1, pp. 26-36, 2005.

[33] PALERMO, E., "**What is Selective Laser Sintering**," [Online]. Available: https://www.livescience.com/38862-selective-laser-sintering.html. [Accessed 02 2020].

[34] YAP, Y, C.; CHUA, K, C.; DONG, L, Z.; LIU, H, Z.; ZHANG, Q, D.; LOH, E, L.; and SING, L, S., "**Review of selective laser melting: Materials and applications**," *Applied Physiscs Reviews,* vol. 4, no. 2, pp. 1-20, 2015.

[35] SCHOLZE, H., "**Glas, Natur, Struktur un Eigenschaften**", Springer-Verlag, 1977.

[36] MONTANEZ, C., "**What does it take to make opaque ceramics transparent**," [Online]. Available: https://www.preciseceramic.com/blog/what-does-it-take-to-make-opaque-ceramics-transparent/. [Accessed 03 2020].

[37] WACKER, C., "**Pyrogenic Silica**," [Online]. Available: https://www.wacker.com/cms/en/products/product_groups/hdk.jsp. [Accessed 04 2019].

[38] CHEMICAL, M., "**MKC Silica**," [Online]. Available: https://www.m-chemical.co.jp/en/products/departments/mcc/inorganic-chem/product/1204076_7994.html. [Accessed 04 2019].

[39] HAAS, R, A., "**DURAMAX D-3005 Dispersant**," [Online]. Available: https://nshosting.dow.com/doc-archive/business/pmat/duramax/duramax_d-3005/tds/duramax_d-3005.pdf. [Accessed 01 2020].

[40] DUPONT, "**Methocel A4M**," [Online]. Available: https://www.industrialcellulosics.com/products/methocel/methocel-a4m#ProductSpecs. [Accessed 02 2020].

[41] REZENDE, R.; BARTOLO, J, P.; MENDES, A.; and FILHO, M, R., "**Experimental Characterisation of the Alginate Gelation Process for Rapid Prototyping**," *Chemical Engineering Transactions,* vol. 1, no. 1, pp. 1-7, 2007.

[42] BRITANNICA, "**Polyvinyl Alcohol**," [Online]. Available: https://www.britannica.com/science/polyvinyl-alcohol. [Accessed 03 2020].

[43] DALCHEM, "**Why is consistency and water to plaster ratio so important**," [Online]. Available: https://dalchem.com.au/how-to/why-is-a-consistencya-and-a-water-to-plaster-ratioa-important#:~:text=A%20mixture%20of%201kg%20of,or%20a%202%3A3%20ratio.. [Accessed 09 2020].

[44] CHUA, C, K.; LEONG K, F.; and LIM, C, S.; "**Rapid Prototyping: Principles and Applications**," River Edge, 2010.

[45] REED, S, J., "**Principles of ceramic processing**", John Wiley & Sons, 1995.

[46] AHN, D.; KIM, H.; and LEE, S., "**Fabrication direction optimization to minimize post-machining in layered manufacturing**," *International Journal of Machine Tools and Manufacture,* vol. 47, no. 3, pp. 593-606, 2007.

[47] DEVILLE, S., "**Freeze-Casting of Porous Ceramics: A Review of Current Achievements and Issues**," *Advanced Engineering Materials ,* vol. 10, no. 3, pp. 155-169, 2008.

[48] HEANEY, F, D., "**Vacuum sintering**," *Sintering of Advanced Materials ,* vol. 1, no. 1, pp. 189-221, 2010.

[49] SARTORIUS, "***Manual of Massing Applications",*** 1999.

[50] WASSILKOWSKA, A.; CZAPLICKA-KOTA, A.; ZIELINA, M.; and BIELSKI, A.; "**An Analysis of the Elemental Composition of Micro-samples using EDS Tecnhique**," *Technical Transactions,* pp. 133-148, 2014.

[51] VENEZIA, M.; PAROLA, L,V.; LONGO, A.; and MARTORANA., "**Effect of Alkali Ions on the Amorphous to Crystalline Phase Transition of Silica**," *Journal of Solid State Chemistry,* vol. 161, no. 1, pp. 373-378, 2001.

[52] SANTOS, C, B., "***Influência do Jateamento com Alumina nas Propriedades Ópticas e Mecânicas de Zircônias Monolíticas Multicamadas usadas em Próteses Dentárias,"*** Florianópolis, 2019.

[53] LEDIC, K, L.; MAJNARIC, I.; MILARDOVIC, S.; ORTOLAN, S.; SPALJ, S.; STEFANCIC, S.; and MEHULIC, K., "**Analysis of Translucency Parameter of Glass-Ceramics Fabricated by Different Techniques**," *Acta Stomatol Croat,* vol. 49, no. 1, pp. 27-35, 2015.

[54] MINOLTA, K., "**Identifying Color Differences Using L*a*b or L*C*H Coordinates**," KONICA MINOLTA, [Online]. Available: https://sensing.konicaminolta.us/blog/identifying-color-differences-using-l-a-b-or-l-c-h-coordinates/. [Accessed 03 2020].

[55] MORAES, G, E.; SANGIACOMO, L.; STOCHERO, P, N.; ARCARO, S.; BARBOSA, R, L. LENZI, A.; SILIGARDI, C.; OLIVEIRA, N, P, A., "**Innovative thermal and acoustic insulation foam by using recycled ceramic shell and expandable styrofoam (EPS) wastes**," *Waste Management,* vol. 89, no. 1, pp. 336-344, 2019.

[56] ZHU, C.; and SMAY, E, J., "**Thixotropic rheology of concentrated alumina colloidal gels for solid freeform fabrication**," *Journal of Reology,* vol. 55, no. 3, pp. 655-672, 2011.

[57] MORENO R., "**Reologia de Suspensiones Ceramicas**," Madrid: C.S.I.C. Madrid, 2005.

[58] PAAR, A., "**The Influence of particles on suspension rheology**," [Online]. Available: https://wiki.anton-paar.com/en/the-influence-of-particles-on-suspension-rheology/. [Accessed 07 2020].

[59] SÁNCHEZ, D, L, J., "***Rheological studies and 3d extrusion-based printing of nanocomposite hydrogels",*** Campinas, 2018.

[60] DAMBY, D, E.; LLEWELLIN, W.; HORWELL, C, J.; WILLIAMSON, B, J.; NAJORKA, J.; CRESSEY, G.; CARPENTER, M., "T**he a–b phase transition in volcanic cristobalite," *Journal of Applied Crystallography,"*** vol. 47, no. 4, pp. 1205-1215, 2014.

[61] NANOTECNOLOGY, I, N., "**What's So Special about the Nanoscale?**," [Online]. Available: https://www.nano.gov/nanotech-101/special#:~:text=Properties%20of%20materials%20are%20size,the%20size%20of%20the%20particle.. [Accessed 07 2020].

[62] ANTONIAMMAL, P.; and ARIVUOLI, D., "S**ize and Shape Dependence on Melting Temperature of Gallium Nitride Nanoparticles**," *Journal of Nanomaterials,* vol. 2012, no. 1, pp. 1-11, 2012.

[63] FALK, G.; SHINHE, G, P.; TEIXEIRA, L, B.; MORAES, E, G.; DE OLIVEIRA, N, A, P., "**Synthesis of silica nanoparticles from sugarcane bagasse ash and nano-silicon via magnesiothermic reactions**," *Ceramics International,* vol. 45, no. 1, pp. 21618-21624, 2019.

[64] KLEIN, L.; APARICIO, M.; JITIANU, A., "**Handbook of Sol-Gel Science and Technology**," 2018.

[65] MOURHLY, A.; KHACHANI, M.; EL HAMIDI, E, A.; KACIMI, M.; HALIM, M.; ARSALANE, S., "**The Synthesis and Characterization of Low-Cost Mesoporous Silica SiO2 from Local Pumice Rock**," *Nanomaterials and Nanotechnology,* vol. 35, no. 5, pp. 1-7, 2015.

[66] XUE, S-H.; XIE, H.; PING, H.; LI, Q-C.; SU, B-L.; FU, Z-Y., "**Induced transformation of amorphous silica to cristobalite on bacterial surfaces**," *RSC Advances,* vol. 88, no. 5, pp. 71844-71848, 2015.

[67] BRENEMAN, C, R.; and HALLORAN, W, J., "**Kinetics of Cristobalite Formation in Sintered Silica**," *Journal of the American Ceramic Society,* vol. 97, no. 7, pp. 2272-2278, 2014.

[68] COLE, S, S., "**The Conversion of Quartz into Cristobalite Below 1000 C and some Properties of Cristobalite Formed**," *Journal of the American Ceramic Society,* vol. 18, no. 1, pp. 149-154, 1935.

[69] ZHAO, T; QIN, Y; WANG, B; YANG, J-F., "I**mproved densification and properties of pressureless-sintered lithium disilicate glass-ceramics**," *Materials Science & Engineering A,* vol. 620, pp. 399-406, 2015.

[70] MORAES, G, E; LI, D; COLOMBO, P; SHEN, Z., "**Silicon nitride foams from emulsions sintered by rapid intense thermal radiation**," *Journal of the European Ceramic Society,* vol. 35, no. 1, pp. 3263-3272, 2015.

[71] PRADO, O, M.; and ZANOTTO, D, E., "**Glass sintering with concurrent crystallization**," *Académie des sciences,* pp. 773-786, 2002.

[72] SOARES, P, J.; SANTOS, E, J.; CHIERICE, O, G.; CAVALHEIRO, T, G, E., "**Thermal behavior of alginic acid and its sodium salt**," *Eclética Química,* vol. 29, no. 2, pp. 57-64, 2004.

[73] NAIR, M, R.; BINDHU, B.; REENA, L, V., "**A polymer blend from Gum Arabic and Sodium Alginate - preparation and characterization**," *Journal of Polymer Research,* vol. 27, no. 6, pp. 1-7, 2020.

[74] PENG, Z.; and KONG, X, L., "**A thermal degradation mechanism of polyvinyl alcohol/silica nanocomposites**," *Polymer Degradation and Stability,* vol. 92, no. 6, pp. 1061-1071, 2007.

[75] EL-DIDAMONY, H.; EL-FADALY, E.; AMER, A, A.; ABAZEED, H, I., "**Synthesis and characterization of low cost nanosilica from sodium silicate solution and their applications in ceramic engobes**," *Boletín de la Sociedad Española de Cerámica y Vidrio,* vol. 161, no. 1, pp. 1-13, 2019.